Spring 5-1-2017

Assembly of ERMES Subunit Mdm12 and its Interaction with Synthetic Lipid Bilayers

Adrian Coscia
University of Connecticut - Storrs, adrian.coscia@uconn.edu

Assembly of ERMES Subunit Mdm12 and its Interaction with Synthetic Lipid Bilayers

Adrian Coscia

June 1, 2017

University of Connecticut

University Scholar/Honors Program

Major Advisor: Dr. Nathan Alder

Associate Advisor: Dr. Victoria Robinson

Associate Advisor: Dr. Debra Kendall

Abstract

Assembly of ERMES Subunit Mdm12 and its Interaction with Synthetic Lipid Bilayers

Adrian Coscia, University Scholar Program

University of Connecticut
2017

The endoplasmic reticulum—mitochondria encounter structure (ERMES) is a tethering complex that mediates the close apposition of ER and mitochondrial membranes. The ERMES complex consists of at least four proteins: the ER transmembrane protein Mmm1, the mitochondrial outer membrane (OM) protein Mdm34, the OM β-barrel protein Mdm10, and the cytosolic protein Mdm12. Accumulating evidence suggests that the ERMES complex provides the molecular basis for non-vesicular phospholipid transport between the ER and mitochondria. Yet how these subunits assemble into a quaternary membrane tether is poorly understood, and the mechanism of ERMES-mediated phospholipid transport has yet to be revealed. Both of these aspects are necessary prerequisites for developing a thorough picture of not only lipid transport at ER—mitochondria contact sites, but of non-vesicular lipid transport in general. Here we show that full-length Mdm12 of *S. cerevisiae* exists primarily as a disulfide-mediated dimer in dynamic equilibrium. We also demonstrate novel features of Mdm12—bilayer interaction, in particular that Mdm12 induces fusion, lysis, solubilization, and aggregation of synthetic lipid bilayers. The results show that the reductant DTT and calcium both modulate the kinetics of Mdm12 lipid binding. Structural aspects of Mdm12 lipid-binding specificity are also addressed by *in silico* phospholipid docking.

Acknowledgements

To my lifeline: my parents, brothers, and sister who inspire me to live and work with vitality and curiosity. For always being keen to know what I was learning and how my work was progressing, for being involved, and for sharing my excitement.

To Ana. For her support, faith, and selflessness. Because she always understood without asking, believed without hesitation, and always asked the perfect questions.

Thank you Dr. Nathan Alder for guidance, support, advice, and every opportunity. For teaching me to be a scientist, and giving me a home at the University of Connecticut. Every success and opportunity that I've been afforded thus far, and any I may be afforded in the future, is because you gave me a chance.

Thank you to everybody who I have been fortunate to work with on the ERMES project: Dr. Victoria Robinson, Dr. Heidi Erlandsen, Nathan Sanford, and Dylan Laprise. The opportunity to work with you all has shown me the face of perseverance in research, and how to adapt to new challenges and continue moving forward.

I am also grateful to the faculty who have also helped me with this project: Dr. Debra Kendall for being a member of my committee, Dr. Eric May for giving me the opportunity to develop my interest in molecular dynamics and simulation, and Dr. James Cole for the analytical ultracentrifugation work.

And last but certainly not least, everybody working in the Alder Lab: Ketan Malhotra, Matthew Greenwood, Murugappan Sathappa, Arnab Modak, Dylan Laprise, Melissa Skoryk, Sally Chamberland, Tess Decater, Wayne Mitchell, and Emily Ng. I am grateful for being able to learn and spend time with you all.

Table of Contents

List of Figures

List of Tables

Introduction

I. The Endoplasmic Reticulum-Mitochondria Junction

Many processes within eukaryotic cells depend on dynamic membrane-bound organelles that segregate specific metabolic processes into compartmentalized microenvironments. Yet cells must also choreograph the transport of proteins, signaling molecules, lipids, and other metabolites between sets of organelles for appropriate function. Intracellular membrane contact sites (MCS) were first identified by electron microscopy as tightly coordinated associations between organelles[1]. In particular, specialized domains of the endoplasmic reticulum (ER), termed mitochondrial-associated membranes (MAMs), form zones of close (~10-50 nm) apposition with the mitochondrial outer membrane (OM)[1-5] (**Fig. 1A**). These junctions play a number of critical roles in signaling, metabolism, and organelle dynamics that require coordination between the ER and mitochondria.

Of particular interest, lipid biogenesis requires the transport of lipids between the ER (the major site of lipid synthesis) and the mitochondrion (**Fig. 1A**, *left*). Mitochondria contain

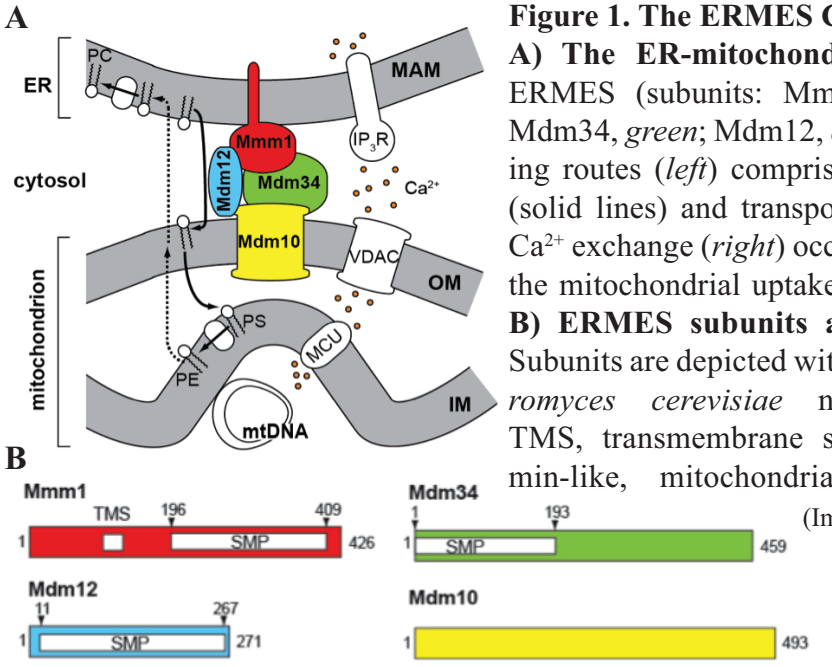

Figure 1. The ERMES Complex
A) The ER-mitochondrial junction tethered by ERMES (subunits: Mmm1, *red*; Mdm10, *yellow*; Mdm34, *green*; Mdm12, *cyan*). Phospholipid trafficking routes (*left*) comprise transport to mitochondria (solid lines) and transport to the ER (dotted lines). Ca^{2+} exchange (*right*) occurs from the IP_3R channel to the mitochondrial uptake machinery (VDAC/MCU). **B) ERMES subunits and domain organization.** Subunits are depicted with relevant residues (*Saccharomyces cerevisiae* numbering). Abbreviations: TMS, transmembrane segment; SMP, synaptotagmin-like, mitochondrial lipid binding protein. (Image courtesty of Dr. Nathan Alder)

enzymes necessary to synthesize some resident phospholipids [e.g. phosphatidic acid (PA), phosphatidylethanolamine (PE), phosphatidylglycerol (PG) and cardiolipin (CL)], but other lipids must be imported from their primary site of synthesis on the ER/MAM membrane[6]. For instance phosphatidylserine (PS) first synthesized on the ER is decarboxylated to PE in the mitochondrial inner membrane (IM) and trafficked back to the ER, where it can be further modified into phosphatidylcholine (PC)[7] (**Fig. 1A**). PC and PE are the two most abundant phospholipids in many biological membranes, and consequently several organisms depend on PS decarboxylation in mitochondria as the major source of PE necessary for appropriate function. Importantly, because mitochondria are not part of the endomembrane system, this bidirectional lipid transport must be non-vesicular[8]. Clearly, this bidirectional lipid trafficking is a fundamental process in organellar biogenesis.

The second preeminent function of the ER-mitochondria contact site is interorganellar Ca^{2+} signaling (**Fig. 1A**, *right*). Mitochondrial Ca^{2+} uptake is critical for cellular Ca^{2+} homeostasis, the regulation of mitochondrial enzymes, and has been linked to pathologies such as cancer, Alzheimer's disease, and Parkinson's disease[9-14]. Upon stimulus, transmembrane IP_3 receptors (IP_3R) release Ca^{2+} stored in the ER, forming microdomains of high calcium concentration (20-40 μM) in close proximity (~15 nm) to ER-mitochondria contact sites[15-17]. Ca^{2+} uptake at the mitochondrial OM is mediated by the non-specific voltage-dependent anion channel (VDAC), which is coupled to the inner membrane Ca^{2+} uniporter (MCU)[18-20]. Notably, because the affinity of MCU for Ca^{2+}(20-30 μM) is lower than cytosolic Ca^{2+} concentration, these microdomains are required for MCU-mediated response[16, 17, 18]. It follows that distance plasticity between juxtaposed membranes may be important in regulating mitochondrial Ca^{2+} response[5].

II. The ERMES Complex

In 2009 a synthetic biology screen in *Saccharomyces cerevisiae* led to the identification of the ER-mitochondria encounter structure (ERMES), a tethering complex that mediates ER-mitochondrial association[21]. The ERMES complex is localized to discrete punctae at contact sites and consists of at least four proteins: the ER-anchored protein Mmm1, the mitochondrial protein Mdm34, the OM β-barrel protein Mdm10, and the cytosolic protein Mdm12 (**Fig. 1A**). A subsequent study identified the Ca^{2+}-binding Miro GTPase Gem1 as an integral and regulatory component of ERMES[22]. In addition to its conspicuous role as a membrane tether, initial genetic interaction screens and biochemical studies implicated the ERMES complex in lipid transport, Ca^{2+} exchange, protein transport, establishment of mitochondrial morphology and mitochondrial division, and inheritance of mitochondrial DNA[23-27]. However, because ER-mitochondria contact sites are dynamic structures with several co-localized multisubunit complexes, it has proven difficult to discriminate between direct and indirect ERMES functions. For example, the role of ERMES in PS transfer has been controversial, confounded by redundancy in lipid transport mechanisms between mitochondria and the rest of the cell[23, 26, 32].

Bioinformatic and structural analyses also support the idea that ERMES plays a role in lipid trafficking. SMP (synaptotagmin-like, mitochondrial and lipid-binding protein) domains have been identified in Mdm12, Mdm34, and Mmm1[28] (**Fig. 1B**). SMP domain-containing proteins have been placed within the TULIP (tubular lipid-binding protein) superfamily of lipid / hydrophobic ligand-binding proteins, of which several protein structures are known[29]. In known TULIP structures with bound lipids, lipid acyl chains bind to the SMP channel lumen whereas lipid head groups lie outside the channel[29]. A recently published crystal structure confirmed the SMP domain of Mdm12 binds phospholipids in this manner[30] (**Fig. 2A**).

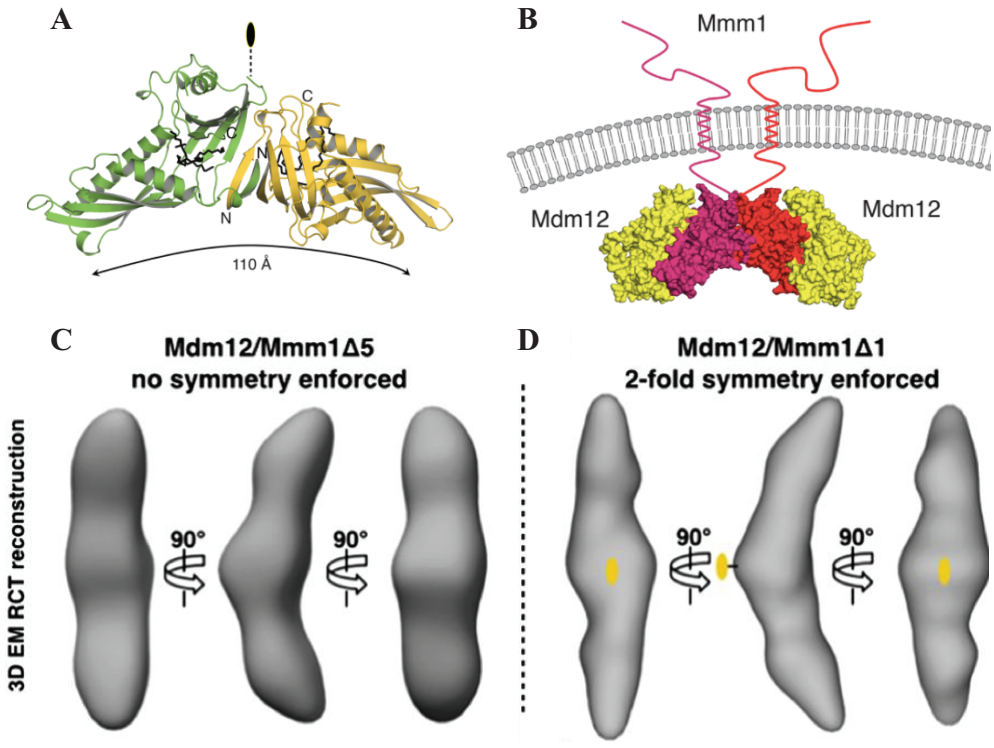

Figure 2. Putative Structure of Mdm12-Mmm1 Ternary Complex
A) Crystal structure of Mdm12 dimer from *S. cerevisiae* refined to 3.1 Å resolution. Disordered loop (74-113) and C-terminal residues (268-271) not shown. Bound lipids are depicted by black stick models.
B) Putative Mdm12-Mmm1 assembly. Mmm1 (magenta/red) homodimer anchored to ER membrane shown binding Mdm12 (yellow) monomers *via* tail contacts distal to Mdm12 dimer interface.
C) Heterotetramer of Mdm12/Mmm1Δ5 (Mmm1Δ1-122) by EM random conical tilt (RCT) reconstruction to 35 Å resolution.
D) Heterotetramer of Mdm12/Mmm1Δ1 (Mmm1Δ1-161) by EM RCT reconstruction with applied two-fold symmetry to 17 Å resolution. Envelope has dimensions of ~210 x 45 x 35 Å.

Panels A/B adapted from Jeong H., et al. 2016. (ref. 30)
Panels C/D adapted from AhYoung A.P., et al. 2015. (ref 31)

Biochemical analysis and EM reconstruction further suggest subunits Mdm12 and Mmm1 assemble into higher-order structure *via* SMP domain-mediated interactions, although the structural basis of this assembly remains unknown[31] (**Fig. 2C and D**). Moreover, both Mdm12 and Mmm1 have been shown to be *bona fide* lipid-binding proteins with a preference for

PC, and to a lesser extent PI[30,31]. However, the lipid-binding properties and the assembly of ERMES subunits are still poorly understood. Additionally, no high-resolution structure of Mmm1, Mdm34, Mdm10, or any ERMES components in complex has been published.

III. Assembly and Lipid-Binding of Mdm12

Lipidomic and biochemical studies addressing Mdm12 lipid-binding specificity have demonstrated that Mdm12 capably binds several different species of phospholipids with appreciable affinity. Independent studies using quantitative mass spectrometry (MS) have shown that Mdm12 expressed in *Escherichia coli* co-purifies with predominantly PE and PG (~80% and ~15% respectively)[30,31]. Displacement assays also demonstrate that PC, PE, PG, and to a lesser extent PI, all bind Mdm12 *in vitro*. Interestingly, MS analysis of Mdm12 incubated with liposomes of native yeast phospholipid composition revealed a two-fold enrichment of bound PC (~60%) relative to native composition (~27%), suggesting PC may be an endogenous ligand *in vivo*[31]. However, these *in vitro* biochemical studies stand in apparent contradiction to the finding that the ERMES complex specifically transports PS[23,32].

Recently published crystal structures of Mdm12 from *S. cerevisiae* revealed a dimer with an elongated tubular structure containing bound phospholipids[30] (**Fig. 2A**). The SMP domain of the Mdm12 monomer closely resembles the topology of SMP domains in related proteins of known structure (**Fig. 3)**. As in E-SYT2 the SMP domains in Mdm12 dimerize, whereas other members of the TULIP superfamily (e.g. BPI and CETP) contain two tandem SMP domains constituted by a single monomer[33-35]. The full-length of structure of Mdm12 details a unique β1 domain swap that mediates self-assembly at the dimerization interface. Highly conserved β1-

strands from each Mdm12 monomer form an intercalated hydrogen-bonding network between the β1- and β2-strands of the respective adjoining monomer (**Fig 3A**). This is a distinctive feature of Mdm12 not yet observed in any other SMP domain-containing proteins, suggesting that Mdm12 lipid binding may be governed by unique dynamics. For example, Mdm12 β1-strand mutants bind lipid with greater apparent affinity[30]. It is possible that Mdm12 monomer-dimer equilibrium serves some role in the dynamic organization of MAMs as it exists *in vivo*.

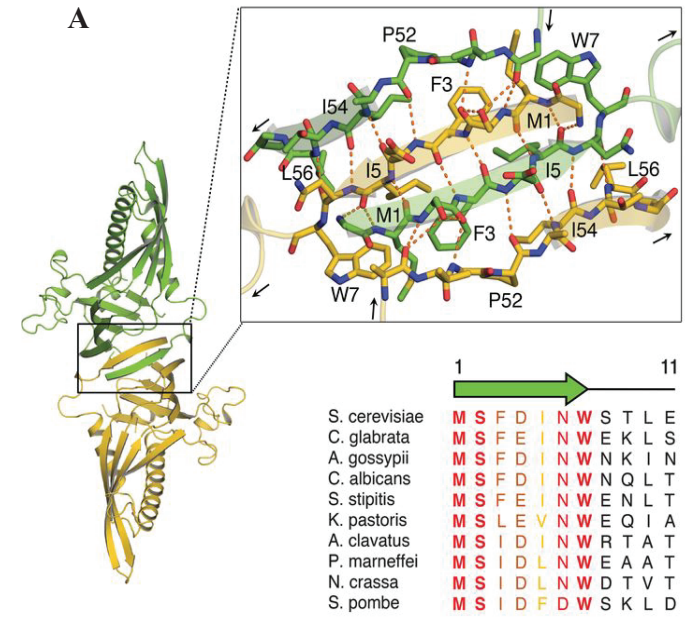

Figure 3. Comparison of Mdm12 to known TULIP Superfamily Proteins. A) Dimer interface of Mdm12 mediated by a β1-domain swap (inset) is unique among SMP domain-containing proteins. Sequence conservation of the β1-strand (residues 1-7) are shown for ten orthologs. **B) Known TULIP proteins** are structurally similar to Mdm12 [(E-SYT2, RMSD: 5.71), (CETP, RMSD: 4.47), (BPI, RMSD: 4.26)]. The dimerization interface of E-SYT2 is characterized by highly conserved helices, in contrast to the β1 domain swap in Mdm12. The two-fold symmetrical interface between the tandem SMP domains of CETP and BPI are both comprised of six-stranded central β-sheets.

Figure adapted from Jeong H., et al. 2016 (ref. 30)

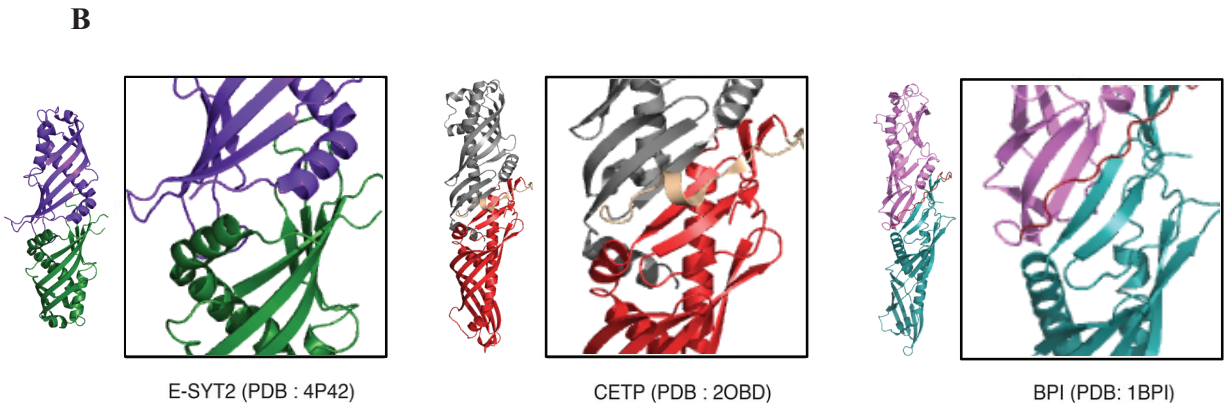

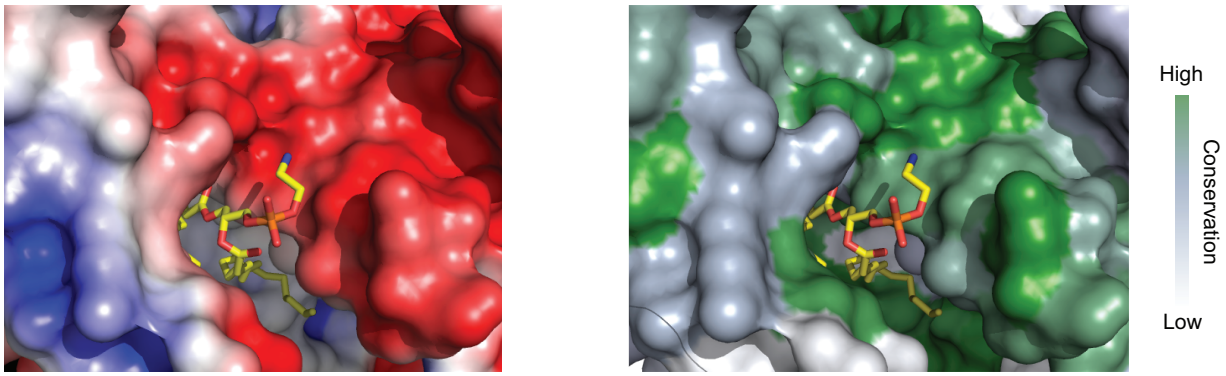

Figure 4. Structural Basis for Glycerophosphilipid Selectivity of Mdm12. Views of structural features suggesting Mdm12 may have preference for phospholipids containing positively charged functional groups in the headgroup region. A surface representation colored by electrostatic potential (left) shows negative charge density proximal to modeled PE head-group. The same view colored by sequence conservation (right) indicates negatively charged residues are highly conserved among Mdm12 orthologs.

Structural evidence also suggests Mdm12 preferentially binds phospholipids containing cationic functional groups. In particular, conserved acidic residues proximal to dimerization interface of Mdm12 contribute to a strong negative surface charge that may provide a structural basis for head-group selectivity (**Fig. 4**). Displacement assays performed with a surface charge mutant corroborated the structure-driven hypothesis. Of note, there was no electron density observed for the C-terminus (also proximal to the head-group of bound lipids) of any Mdm12 monomer in the crystal structure, and whether it plays a dynamic role in lipid binding is unknown. Additionally the authors observed no electron density for non-conserved residues 74-114. A crystal structure of ΔMdm12 (Δ74-114) demonstrated that the major features of full-length Mdm12 are preserved without these residues. Yet despite no apparent sequence conservation, several Mdm12 orthologs contain a corresponding non-conserved sequence of variable length (**Fig. 5**). Although generality may not be drawn from the role of this region of Mdm12 from *S. cerevisiae*, this non-homologous region may contribute to unique plurality of Mdm12 function at membrane contact sites in different species.

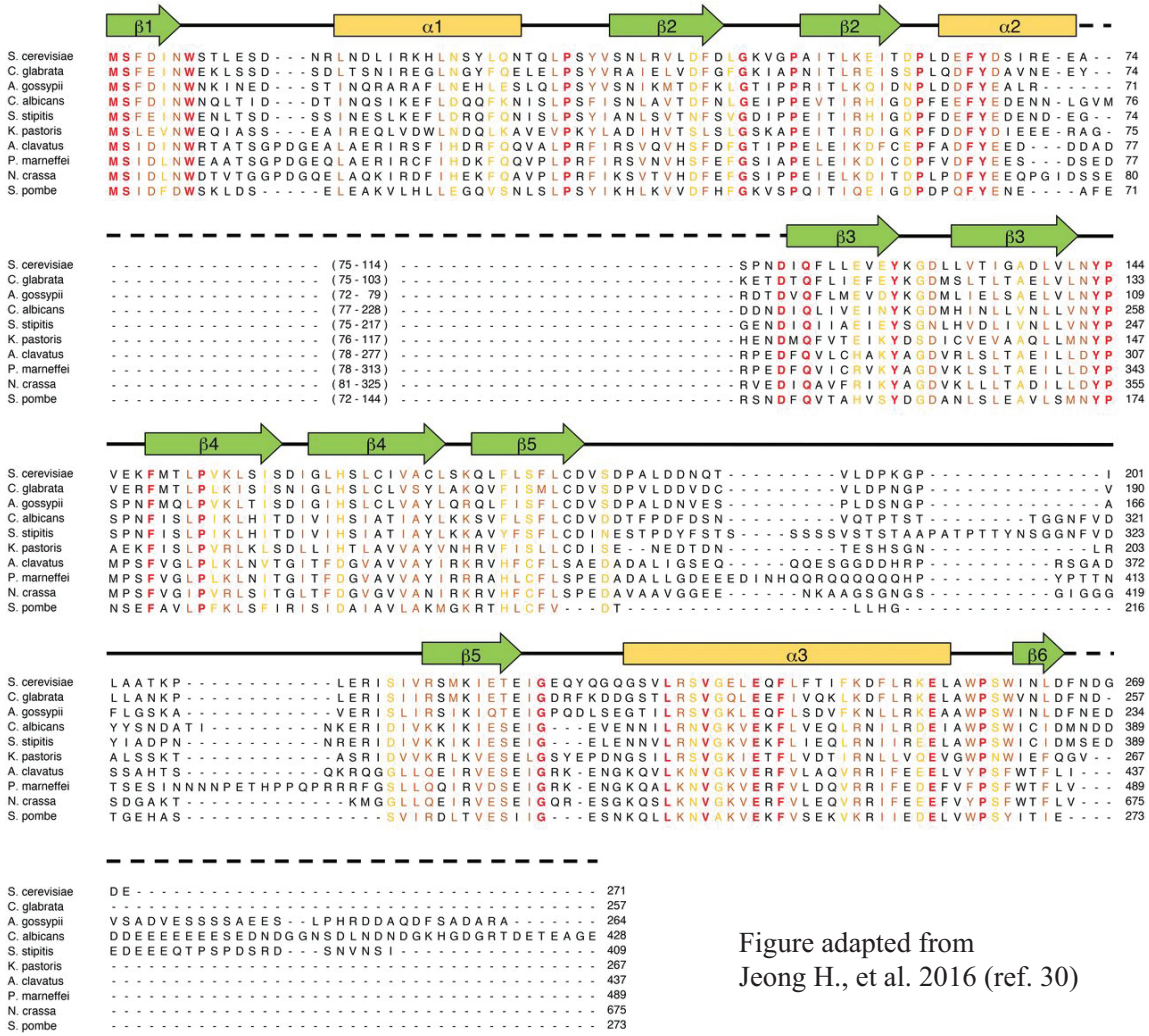

Figure adapted from
Jeong H., et al. 2016 (ref. 30)

Figure 5. Sequence Conservation of Mdm12. Sequence alignment to Mdm12 orthologs in fungi. Completely and highly conserved residues shown in red and yellow, respectively. Secondary structural elements are represented as follows: helices--yellow, strands--green, loops--solid line, disordered--dotted line.

Materials and Methods

I. Cloning and Protein Purification

cDNA encoding full-length Mdm12 WT from *S. cerevisiae* were each cloned into a pET28a vector containing an N-terminal His_6-tag. Mdm12 ΔC92S was generated by site directed mutagenesis of the Mdm12 WT construct, and confirmed by sequencing. Constructs were transformed into *E. coli* BL21 (DE3) cells and grown at 37˚C to an OD_{600} of 0.7 before overnight induction with 1 mM IPTG at 18˚C. Cells were then harvested by ultracentrifugation, resuspended in lysis buffer (20 mM HEPES [pH 7.4], 100 mM NaCl) supplemented with 1 mM PMSF, and lysed by probe sonication at 4˚C. Mdm12 was purified at 4˚C using Ni-NTA chromatography, followed by gel filtration chromatography (Superdex 75 10/300 GL, GE Healthcare) and eluted in lysis buffer. Mdm12 WT ΔCa^{2+} (calcium removed) was subject to dialysis against an EDTA-containing buffer (20 mM HEPES [pH 7.4], 100 mM NaCl, 5 mM EGTA) prior to gel filtration. Protein was concentrated by centrifugation and flash frozen using liquid nitrogen as needed.

II. Analytical Ultracentrifugation (AUC)

Sedimentation velocity experiments were conducted at either 20˚C or 5˚C and centrifuged 40,000 RPM. Measurements were taken using an analytical ultracentrifuge (Beckman-Coulter XL-I) equipped with absorbance optics. Samples were first loaded into double sector cells fitted with quartz windows, equilibrated in the centrifuge for ~1 hour at the respective temperature, and then accelerated to the final rotor speed (40,000 RPM). Absorbance measurements at 280 nm were acquired at 4.5 minute intervals for ~9.5 hours. The experiment was performed at multiple concentrations for each experiment. Continuous sedimentation

coefficient distribution, c(s), analysis was performed using a resolution of 0.05S and maximum entropy regularization with a 95% confidence limit to determine the sedimentation coefficients for each species in the sample.

III. Liposome preparation and characterization.

All lipids (POPC, POPE, TOCL, NBD-PE) were provided as chloroform stocks from Avanti Polar Lipids. Lipids were dried under a nitrogen stream for 20 min and lipids films were subsequently desiccated overnight. Lipids were hydrated in reaction buffer (20 mM HEPES [pH 7.5], 100 mM NaCl) for 30 min, and extruded (≥13 times) manually using a mini-extruder at room temperature through a 0.1μm polycarbonate membrane (Avanti Polar Lipids, USA) to form large unilamellar vesicles (LUVs). The final total lipid concentration of the extruded LUVs was measured using an ammonium ferrothiocyanate colorimetric analysis[37]. Dynamic light scattering measurements were obtained from backscatter intensities measured at 25˚C using a Zetasizer Nano ZS (Malvern Instruments, Worcestershire, U.K.) as described below. The size and morphology of 100% NBD-PE LUVs was confirmed by transmission electron microscopy (TEM), also described below.

IV. Native PAGE Analyses

Effect of reductant (DTT). Purified Mdm12 WT and Mdm12 ΔC92S (16.2 μM) in reaction buffer was mixed with increasing concentrations of DTT and incubated with an equimolar ratio of NBD-PE(18:1) (100% NBD-PE LUVs prepared as described in appendix A.II) at room temperature for 45 min. Reactions were resolved on a 12% acrylamide native gel

and Mdm12 was visualized by Coomassie stain. Fluorescence was visualized by FITC scans using a PharosFXPlus Gel Imager (Bio-Rad) and Image Lab 3.0 software.

Effect of calcium. Purified Mdm12 ΔCa^{+2} and calcium-reintroduced Mdm12 ΔCa^{+2} (5.8 μM) were pre-incubated with reaction buffer and calcium-supplemented buffer (20 mM HEPES [pH 7.4], 100 mM NaCl, 500 μM $CaCl_2$), respectively, for 5 min. Samples were then mixed with increasing concentraitons of DTT and incubated with an equimolar ratio of NBD-PE(18:1) (100% NBD-PE LUVs prepared as described in appendix A.II) at room temperature for 45 min. Reactions were resolved on a 12% acrylamide native gel and in-gel fluorescence was visualized using a PharosFXPlus Gel Imager (Bio-Rad) and Image Lab 3.0 software.

V. Docking with Glide

Preparation of Mdm12. The crystal structure of full-length Mdm12 (PDB 5GYD) was prepared using the Protein Preparation Wizard workflow in Maestro (Schrödinger). Hydrogen atoms were added to the biological unit structure during preprocessing, however missing loops remained omitted. Heteroatom states were generated using Epik (pH: 7.0 ± 2.0). Hydrogen bond assignments were optimized and restrained minimization (OPLS3 Force Field) was performed to yield the final prepared structure.

Ligand library generation and preparation. A phospholipid library was manually curated for Mdm12 docking. SDF files were downloaded from the LIPID Metabolites and Pathways Strategy database (LIPID MAPS).

TABLE I. LIPID LIBRARY FOR GLIDE DOCKING

Phospholipid	Fatty Acid Composition
PC (32:1)	(14:0/18:2(11Z,14Z)) (14:0/18:2(9Z,12Z)) (14:1(9Z)/18:1(9Z)) (16:1(9Z)/16:1(9Z))
PE (34:2)	(16:1(9Z)/18:1(9Z))
PG (34:1)	(16:0/18:1(9Z)) (18:1(9Z)/16:0)
PI (32:1)	(14:0/18:1(9Z)) (14:1(9Z)/18:0) (16:0/16:1(9Z))
PS (34:1)	(16:0/18:1(9Z)) (16:1(9Z)/18:0)

The previously identified[30,31] predominant Mdm12-bound *S. cerevisiae* phospholipid species PC(32:2) and PG(34:1) were included, in addition to PE(34:2), PI(32:1) and PS(34:1). Fatty acid compositions of each respective species naturally present in *S. cerevisae* were included in the library (**Table 1**)[36]. 3-dimensional models of library lipids were subsequently prepared using LigPrep (Schrödinger) with SDF-defined stereochemical contraints. Epik was used to generate ionization states (pH: 7.0 ± 2.0) and OPLS3 used for restrained minimization.

Receptor grid generation. The receptor grid was generated for one monomer (PDB 5GYD//B) of the Mdm12 homo-dimer automatically by identifying the co-crystallized ligand. Ser260 was defined as a rotatable group and the default van der Waals radius scaling factor (1.0) and partial charge cutoff (0.25) were kept and subject to OPLS3 force field. A second grid was generated with a headgroup NOE for subsequent constrained PC docking.

Glide Extra Precision (XP) ligand docking. XP flexible ligand docking was performed using Glide[38] (Schrödinger). Default settings including ligand van der Waals scaling (0.80) and partial charge cutoff (0.15) were used. Post-docking minimization was performed on the ten best poses for each ligand and a maximum of three poses per ligand were reported. Per-residue interaction scores for residues within 12.0Å of the ligand were written to the report file.

VI. Dynamic Light Scattering (DLS)

Mdm12-mediated liposome remodeling. Purified Mdm12 WT (500 µL of 1 µM) was mixed with an equimolar amount of 100% NBD-PE LUVs (500 µL of 1 µM NBD-PE) in a 1.5 mL microfuge tube at room temperature. At each recorded time point of the interaction the sample tube was inverted 5 times to ensure even mixing, and a 60 µL aliquot of sample was loaded into a quartz cuvette. The cuvette was washed between each time point sample.

Measurements were acquired at 25˚C using a ZetaSizer Nano S (Malvern Instruments, UK) with a 4-mW He-Ne laser (λ = 633 nm), and particle sizes were determined by back-scattering at 173˚. Data analysis was performed using DTS Nano software (Malvern Instruments, UK).

VI. Transmission Electron Microscopy (TEM)

LUVs of 100% NBD-PE (~0.9 mM) were plasma cleaned and imaged by negative staining (uranyl acetate), both alone and after brief incubation (~5 min) with Mdm12 WT (10 μM). Images were collected at 18,500-150,000x on a Tecnai 12 G2 Spirit BioTWIN transmission electron microscope (FEI, Oregon, USA) with an acceleration voltage of 80.0 kV.

VII. Fluoresence Titrations and Timecourse

Time course measurements. Fluorescence wavescans of NBD-PE (λ_{ex} = 470 nm, λ_{em} = 500-600 nm) were performed using a Fluorolog 3-22 spectrofluorometer (HORIBA Jobin-Yvon) equipped with a 450-W xenon lamp (λ_{ex} = 470 nm), a photon-counting digital photomultiplier (λ_{em} = 500-600 nm), and double grating excitation and emission monochromators (5 nm bandpass; 5 nm bandpass). 250 μL reactions (20 nM Mdm12 WT; 0.4 μM NBD-PE) with DTT (4 mM) or without, were briefly mixed at room temperature. Samples were then transferred to quartz cuvettes (1 cm pathlength) and wavescans were measured as described above. Wavescans were recorded consecutively at each time point for the duration of the time course, until the fluorescence intensity reached a maximum (2-186 min). Samples were not mixed between consecutive measurements. The fluorescence intensity (cps) at the NBD emission maximum (λ_{ex} = 530 nm) was plotted as a function of time, and fit using non-linear least-squares regression (Kaleidagraph, Synergy Software, PA).

VII. Stopped-flow Fluorescence

Pre-steady-state kinetics experiments were performed with an SX-20 stopped-flow instrument (Applied Photophysics, UK). Samples were excited at 465 nm and emission was detected using a 500 nm long-pass cutoff filter. Mdm12 and NBD-PE LUVs were loaded into a 1.0 mL syringes at double the final reaction concentration, respectively, and equal volumetric mixing ratio of Mdm12: NBD-PE was used. The final concentration of NBD-PE was constant in all experiments (1 μM) and the concentration of Mdm12 was titrated (0.025-2.5 μM). To test the effect of reductant on the kinetics of lipid-binding, Mdm12 WT and Mdm12 ΔCa^{+2} were preincubated (~5 min) with 1 mM DTT before loading and initiating the lipid-binding reaction. For calcium reintroduced experiments, Mdm12 ΔCa^{+2} was preincubated in reaction buffer containing 5 μM $CaCl_2$ for ~5 min before samples were loaded and the lipid-binding reaction was intiated. All experiments were performed in reaction buffer. Measurements were collected for 10, 100, and 1000s reactions and data were analyzed using SX Pro-Data Viewer (Applied Photophysics, UK). Triplicate fluorescent transients from a single experiment were averaged and fit to multiexponential curves, in which an additional exponential term was added to account for photobleaching. The rate of this fixed additional term was determined by NBD-PE—reaction buffer equal-mixing control experiments.

Results

I. Oligomeric State of Mdm12

A construct of full-length Mdm12 containing an N-terminal 6XHis-tag (His-Mdm12) was expressed in *E. coli* and purified as described above. As also observed by Jeong, et al., 2016, the TEV cleavage site was inaccessible to protease and only small amounts of TEV-cleaved Mdm12 could be formed by proteolysis (not shown). This suggests that the fold of the N-terminal region of Mdm12 may occlude the TEV cleavage site. The elution profile of His-Mdm12 shows two distinct species corresponding approximately to the MW of the Mdm12 monomer and dimer (**Fig. 6**). Native PAGE analysis of Mdm12-containing fractions indicates that the distribution of oligomers is dynamic, as either peak fraction redistributes into a dimer/monomer mixture immediately upon elution. A large fraction of Mdm12 appears in earlier fractions suggesting either that there is significant aggregation or that Mdm12 also forms higher-order oligomers.

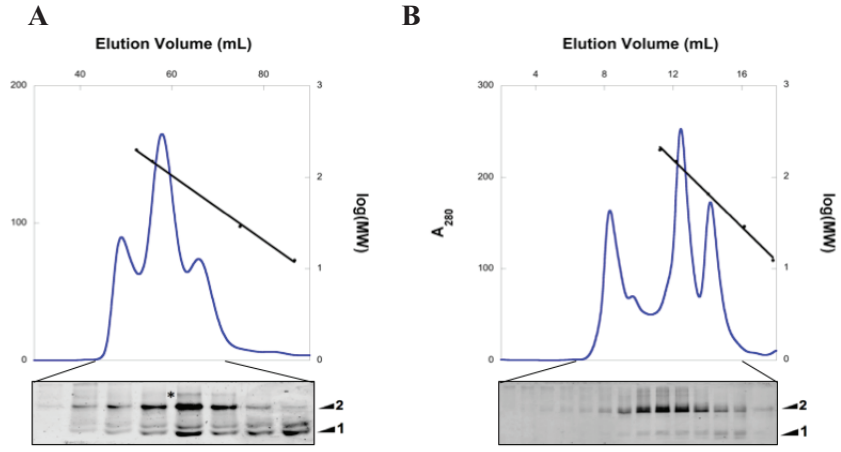

Figure 6. Mdm12 exists as multiple oligomeric states. GFC run at 4˚C on an S75 column **(A)** and at room temperature on an S200 column **(B)** separates Mdm12 into monomer/dimer fractions. Mdm12-containing fractions run on native PAGE indicate this monomer-dimer equilibrium is dynamic as all peak fractions can redistribute into a mixture of monomer (*band 1*) and dimer (*band 2*).

AUC suggests that the dimeric species of Mdm12 is the most abundant oligomer (~85%, $S_{20,w} \approx 4S$) both at low temperature (5˚C) and at room temperature (20˚C) (**Fig. 7**). However at room temperature, Mdm12 exists in monomer/dimer equilibrium whereas a dimer/tetramer mixture is observed at low temperature (**Fig.** 7A). Moreover, both the monomer and tetramer

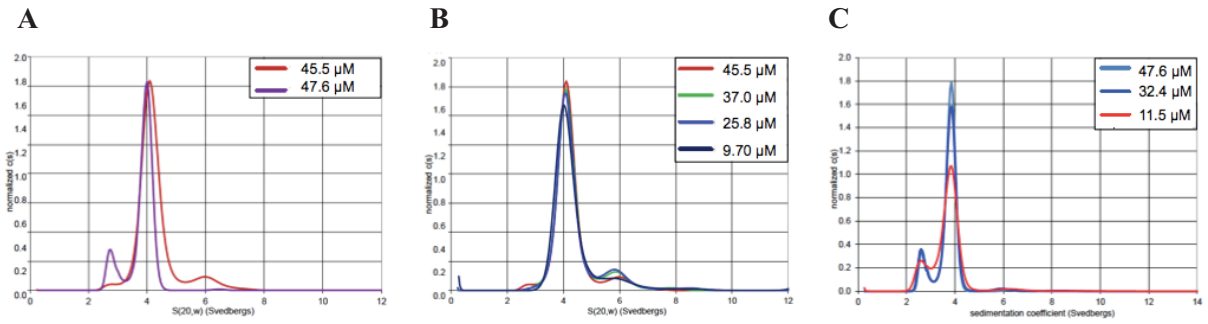

Figure 7. Temperature affects the oligomeric state of Mdm12. (A) Continuous sedimentation coefficient distribution c(s) of Mdm12 at different temperatures as measured by AUC. The molecular weight corresponding to the main peak (s ~ 3.9 Svedbergs) is consistent with that of an Mdm12 dimer. Analysis of c(s) distribution shows no concentration dependence on the distribution of different MW species at low temperature **(B)** or at room temperature **(C)**. Mdm12 exists as a mixture of two species, the monomer and dimer at room temperature, and the dimer and tetramer at low temperature.

comprise 15% of the total sample at high and low temperature, respectively, and remain in constant proportion to the total amount of dimer (85%) (**Table 2**).

TABLE 2. ANALYTICAL ULTRACENTRIFUGATION PARAMETERS

Sample	MW(1) (kDa)	s(1) (Svedbergs)	s(2) (Svedbergs)	[m(2)]/[m(1)]	RMS error (A_{280})
20°C	32.2	2.44	3.83	2.76†	0.013
4°C	61.6	4.06	5.78	0.073‡	0.0136

† Corresponds to an average weight percentage of 15% for the monomer and 85% for the dimer.
‡ Corresponds to an average weight percentage of 87% for the dimer and 13% for the tetramer.

The association state of Mdm12 can be disrupted by the introduction of reductant DTT, suggesting that Mdm12 forms disulfide-mediated oligomers (**Fig. 8A**). Mutagenesis experiments suggest cysteine 92 (Mdm12 ΔC92S) in particular is critical in mediating the formation of the Mdm12 dimer. Mdm12 ΔC92S exists as primarily a monomer even in the absence of DTT, and moreover when pre-incubated with DTT Mdm12 ΔC92S exhibits no change in the distribution of monomer and dimer equilibrium (**Fig. 8B**). In gel FITC scans showing NBD-PE bound to Mdm12 illustrate that both dimer and monomer can capably bind lipids (**Fig. 8A/B,** *NBD-PE*). Self-association of Mdm12 has been previously reported[30,31], however previous results indicate that His-tagged Mdm12 forms only the monomeric species. Moreover our finding that Mdm12

dimerization is disulfide-mediated stands in contrast to structural evidence showing that Mdm12 forms a homodimer mediated by swapping of the highly conserved β1-strand. In the reducing cellular environment it is possible that Mdm12 does not form disulfide-mediated oligomers as it exists in the ERMES complex. On the other hand, there is no structural information currently available for the large disordered loop containing residue C92 (residues 74-114), and given the finding that C92 is important for reversible dimerization it is possible that it may play some role in Mdm12 assembly *in vivo*.

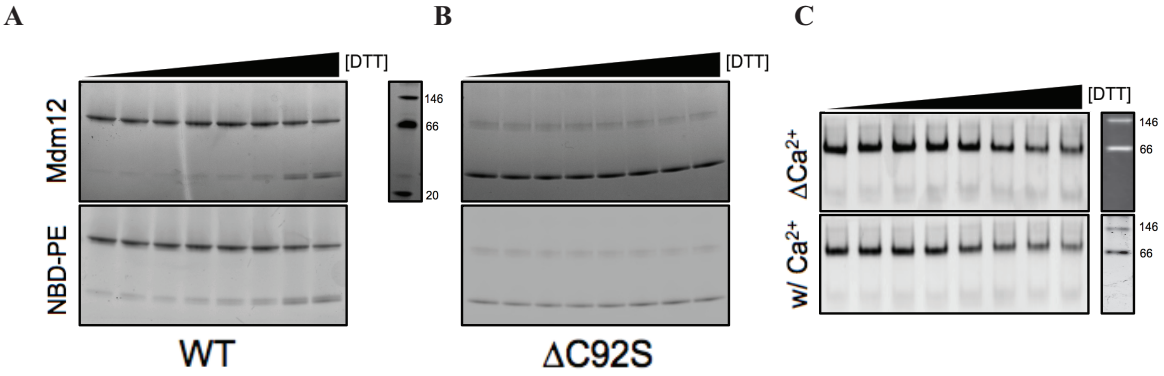

Figure 8. DTT and Ca^{+}affect the oligomeric state of Mdm12. Mdm12 WT **(A)** and Mdm12 ΔC92S **(B)** were incubated with NBD-PE LUVs at increasing DTT concentrations. At high DTT concentrations, the higher MW species (dimer ~66 kDa) is shifted partially to the lower MW species (monomer ~33 kDa) as imaged by coomassie staining. FITC gel images indicate both MW species have bound NBD-PE. Mdm12 Δ C92S exists predominantly as the lower MW species even at low DTT concentration. **(C)** Ca^{2+} potentiates Mdm12 WT sensitivity to DTT. FITC scans of preliminary gels indicate that the higher MW species of Mdm12 ΔCa^{2+} is less responsive to reduction by DTT than Mdm12 ΔCa^{2+} with reintroduced calcium.

Interestingly, calcium may potentiate the effect of DTT on the oligomeric state of Mdm12. FITC scans of preliminary native PAGE gels show that the change in fluorescence intensity of the lipid-bound species of Mdm12 dialyzed in EGTA (Mdm12 ΔCa^{+2}) may be less responsive to DTT than Mdm12 ΔCa^{+2} pre-incubated with calcium ions (**Fig. 8C**). However, FITC scans of both gels show minimal response to treatment with DTT. Also, FITC scans alone are not sufficient to measure possible changes to the oligomeric state of Mdm12. Changes in band intensity may only reflect changes in the ability of Mdm12 to bind lipids, and not

changes in oligomeric state. In subsequent experiments the gels must also be stained to resolve protein bands to ensure that the intensity of the bands measured by FITC also reflect relative amounts of Mdm12.

II. Phospholipid Docking of Mdm12 *in silico*

Glide was used to dock a library of phospholipids into the binding site of Mdm12. The library of candidate glycerophospholipid ligands was manually curated based on the aforementioned MS findings of Mdm12-bound lipid species[30,31] (**Table 1**). Fatty acid composition was selected to mimic acyl chains found naturally in *S. cerevisiae*[36]. Mdm12 (PDB 5GYD) was prepared using the default Protein Preparation Workflow (Schrödinger) and a grid was generated for the lipid-binding site of one monomer of the homo-dimer assembly, defined by identifying the co-crystallized ligand. For the second round of docking specifically with PC, another grid was defined with a NOE constraint to bias docking into generating a pose with the tertiary amine of PC in proximity to the acidic residues hypothesized to play a role in forming favorable interactions with choline headgroup. XP flexible ligand docking was then performed using Glide with default settings. Nearly all generate poses were in the posture observed as in the co-crystallized ligand, wherein the acyl chains lie within the SMP lumen and the headgroup is solvent-exposed (**Fig. 9A**).

Interestingly, the hypothesized *in vivo* ligand (PC) generated the least favorable poses of all species docked (**Fig. 9B**). Moreover, those generated showed an abnormal inverted pose in which one acyl chain docked within the SMP lumen and the other occupied the expected headgroup region, while the choline headgroup formed favorable contacts with the dimerization interface. A second round of docking was performed in which the aforementioned NOE constraints were defined to bias poses such that the choline headgroup was proximal to the

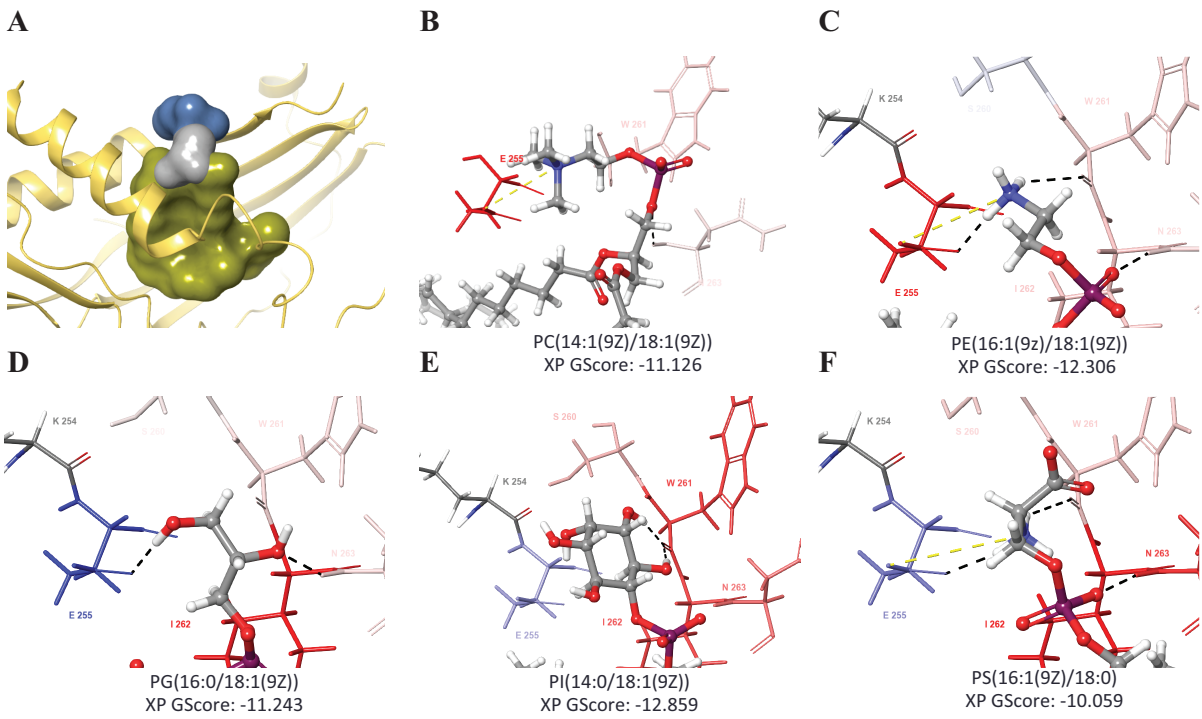

Figure 9. Top poses of Mdm12-docked phospholipd ligands. (A) The overall pose of cocrystallized lipid ligand (PE) with the acyl chains (olive) facing the SMP lumen, and the ethanolamine headgroup (blue) exposed to solvent. The glycerol moeity is shown in gray. Residue-specific interactions (H-bond:black, coulombic interaction:yellow) between the headgroup of the docked phospholipid and the binding site of Mdm12 are shown for **(B)** phosphatidylcholine (PC), **(C)** phosphatidylethanolamine (PE), **(D)** phosphatidylglycerol (PG), **(E)** phosphatidylinositol (PI), and **(F)** phosphatidylserine (PS).

highly conserved, positively charged residues of interest. Only two poses could be generated in the second round of docking, and only with one of three PC species, PC(14:1(9Z)/18:1(9Z)). One of these poses had a highly favorable GlideScore (-11.126) while the other pose was relatively unfavorable (-5.039). It is likely that the lipid-binding site of the Mdm12 is dynamic *in vivo*, and this particular crystallized posture may not be representative of the PC-bound state. Likely a PC-bound state would require a larger width of the lateral seam of the SMP domain proximal to the dimerization interface. Of note, an Mdm12 monomer from this crystal structure alone can easily accommodate a choline headgroup. This is, if repeated with only the monomer PC would likely generate a large number of favorable poses.

PI (14:0/18:1(9Z)) generated the two best poses of all docked ligands (**Fig. 9E**). Although the inositol headgroup is large and non-ionized, it forms extensive polar contacts with the main chain atoms of conserved residues W261, I262, and N263. Of note, the previous MS data indicates that Mdm12 is highly enriched in bound PI species relative to normal cellular concentrations in *S. cerevisiae*. Docking of PG and PS species also generated a large number of poses with favorable XP GlideScores (**Fig. 9D & F**). Similarly, the conserved residues of interest participating in favorable contacts with inositol headgroups also participated in extensive favorable contacts with both PG and PS headgroups. However, no ligands other than PE, and PC in the second round of docking, formed favorable contacts with E255, the highly conserved residue previously hypothesized to specifically play a critical role in headgroup selectivity. In fact, PI, PG, and PS all formed significant *unfavorable* interactions with E255. Perhaps E255 may play a role in headgroup specificity by a mechanism of *negative* headgroup selectivity (forming unfavorable interactions with particular headgroups) rather than by positive selectivity as previously hypothesized.

Docking of the cognate ligand PE generated the most favorable docking scores on average. Notably, the protein sample used to determine the Mdm12 crystal structure was purified from *E. coli*, in which PE composes ~80% of the total lipid composition. The co-crystallized lipid of the structure used for docking was modeled to be a completely saturated species of PE, a species not commonly found *in* vivo. Moreover, MS analyses of lipids bound to Mdm12 purified from *E. coli* have shown that ~80% of bound lipid is indeed PE. Therefore, the binding site used for Glide docking represents a conformation biased for favorable PE docking.

Headgroup specificity, however, is not the primary determinant of favorable docking. Rather, interactions between the SMP lumen and the acyl chain compose the vast majority of

favorable binding interactions (**Fig. 10**). In all cases lipophillic contacts between the acyl chains and hydrophobic residues in the SMP lumen are significantly more abundant than electrostatic interactions between lipid head-groups and the conserved proximal residues (**Fig. 10B & C**). However, poses that had fewer favorable headgroup contacts also had fewer favorable lipophilic interactions and inversely, those with many favorable headgroup contacts also had a large number of favorable lipophilic interactions. Hence, for any given lipid it cannot be said whether the headgroup specifically was the cause for the generation of the favorable pose. Additional docking studies in which the acyl chain is kept constant and in a fixed conformation can be performed to more specifically investigate only the effects of particular lipid headgroups on docking score.

Taken together, multiple lipid ligands generate highly favorable poses within the crystallized binding site and it is likely that Mdm12 binds multiple lipid species as it exists in the ERMES complex *in vivo*. Moreover, this study suggests that headgroup specificity plays a minimal energetic role in Mdm12 lipid binding.

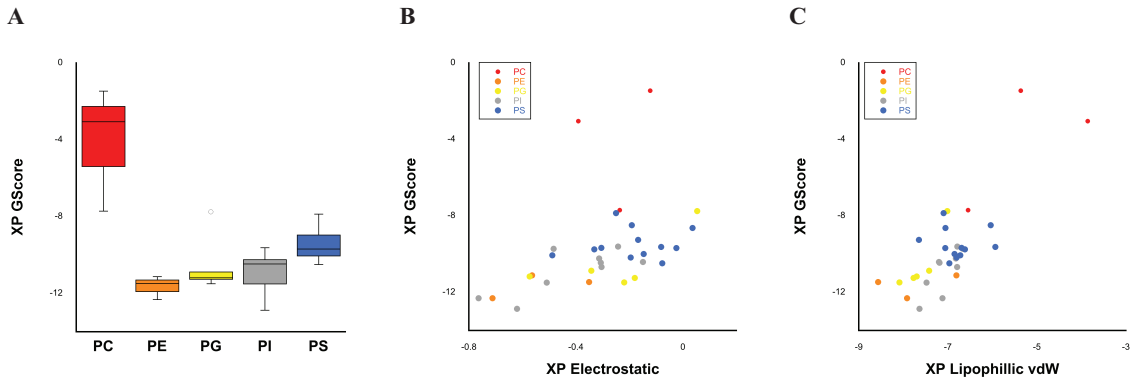

Figure 10. XP Glide docking of glycerophospholipids. (A) Box plot of XP GlideScore by phospholipid shows that multiple lipids dock with highly favorable docking scores except for PC. PE docks with the most favorable score on average and PI docking generated the most favorable pose overall. The XP Glide-Score depends on both electrostatic **(B)** and lipophillic vdW **(C)** interactions between Mdm12 and the docked ligand.

III. Mdm12 Remodels Synthetic Bilayers

The effect of Mdm12 binding on overall liposome size and morphology was assessed by time course DLS experiments and transmission electron microscopy. Mdm12 induced large-scale morphological changes including fusion, tubulation, tethering, and solubilization of 100% NBD-PE liposomes (**Fig. 11**). Prior to interaction with Mdm12, NBD-PE LUVs were monodisperse with an approximate hydrodynamic radius (D_H) of 100nm as measured by DLS, and exhibited normal morphology (**Fig. 11A/E**). DLS also showed that purified Mdm12 alone is solution was also monodisperse (D_H ~1-10 nm) prior to interaction with NBD-PE LUVs.

Upon Mdm12-binding TEM images illustrate dramatic changes in the overall morphology of the LUVs. Moreover, time course DLS experiments suggested that Mdm12 lipid-

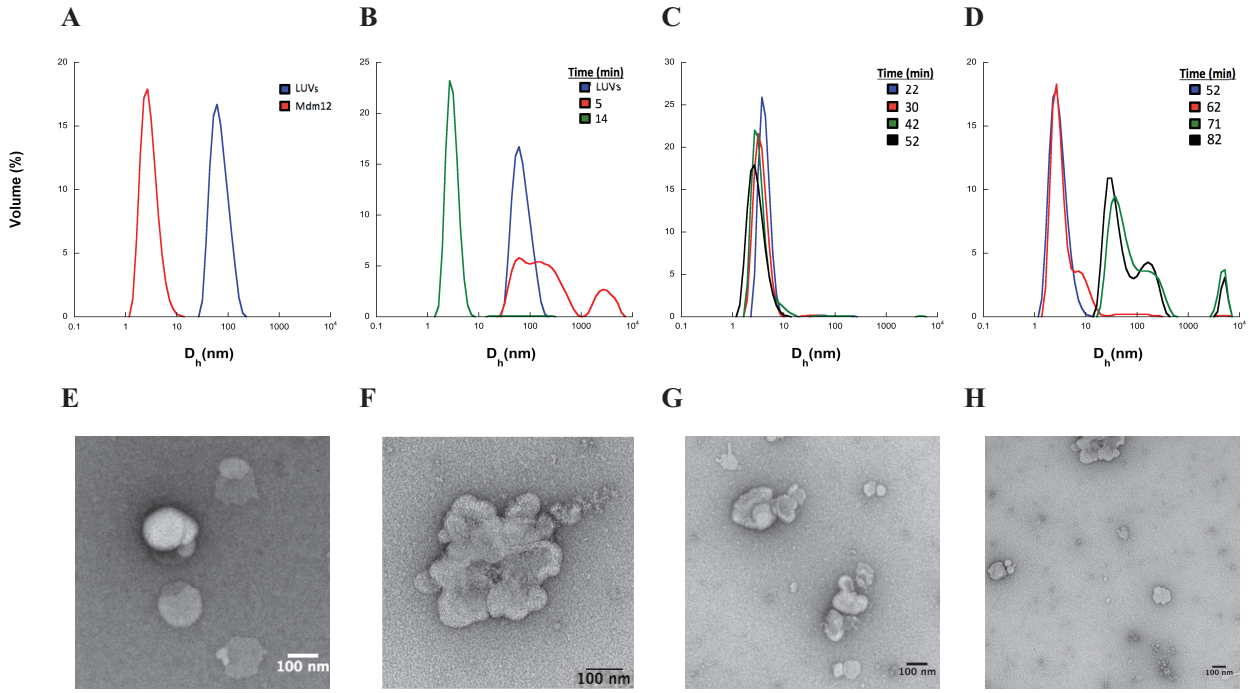

Figure 11. Mdm12 induces vesicle fusion and bilayer reorganization. (A/E) Stable large unilamellar vesicles (LUVs) composed of 100% NBD-PE can be formed in isolation (D_H ~100 nm). **(B)** Upon intial (5 min) interaction with Mdm12 NBD-PE LUVs form aggregates. **(C)** Between 14-63 min interaction the predominant species measured by DLS and visualized by volume PSD is approximately the size of the Mdm12 in isolation (D_H ~1-10 nm). **(D)** Aggregates again begin to form at 71 min and continue to form until reaction equilibrium at 90 min. LUVs and Mdm12 were incubated at equimolar concentrations. **(F-H)** Representative TEM images of the different liposome morphologies induced upon Mdm12 interaction with LUVs are shown.

binding is a complex multi-step reaction, and may be broadly separated into three distinct phases. The first phase occurs upon initial interaction (5 min) at which point liposomes begin to form large aggregates (**Fig. 11C/F**). A second phase is characterized by a sudden decrease of the average particle size (D_H ~1-10nm) in the sample as measured by volume distribution. Interestingly, this is the same size as Mdm12 alone in solution. This second phase is prolonged, and the average particle size in solution remains constant for ~60 min at room temperature (**Fig. 11E/G**). A third and final apparent phase shows a second phase of aggregation, in which the average particle size increases to form three distinct populations (D_H ~50nm, ~100-200nm, and >10μm) (**Fig. 11G**). It cannot be said with certainty whether this size distribution of aggregate is distinct from that formed in the initial aggregation phase.

IV. Kinetics of Mdm12 Lipid Binding

A fluorescence-based approach was used to investigate Mdm12 lipid-binding at finer kinetic resolution. Stopped-flow was used to perform rapid mixing experiments in which Mdm12 and LUVs of 100% NBD-PE were mixed at equal volumes, where the relief of NBD self-quenching was interpreted as a readout for Mdm12—lipid interaction. Stopped-flow results corroborated the findings from DLS experiments, also indicating that Mdm12 interacts with liposomes via a complex multiphasic reaction consisting of at least three different kinetic phases (**Fig. 12**). First, there is an initial rapid phase (~10 ms) and that accounts for only a small increase (<5%) in the overall fluorescence signal (**Fig. 12A**). This is followed by a longer (~1-40 sec) secondary phase, which contributes a much larger proportion of the total fluorescence signal(~50%) (**Fig. 12B**). The reaction never saturated even at the maximum programmable time interval on the stopped-flow apparatus (1000 sec). Rather, the reaction enters a third phase (~50 sec) that appears linear at the timescales measured by stopped-flow, and also contributes

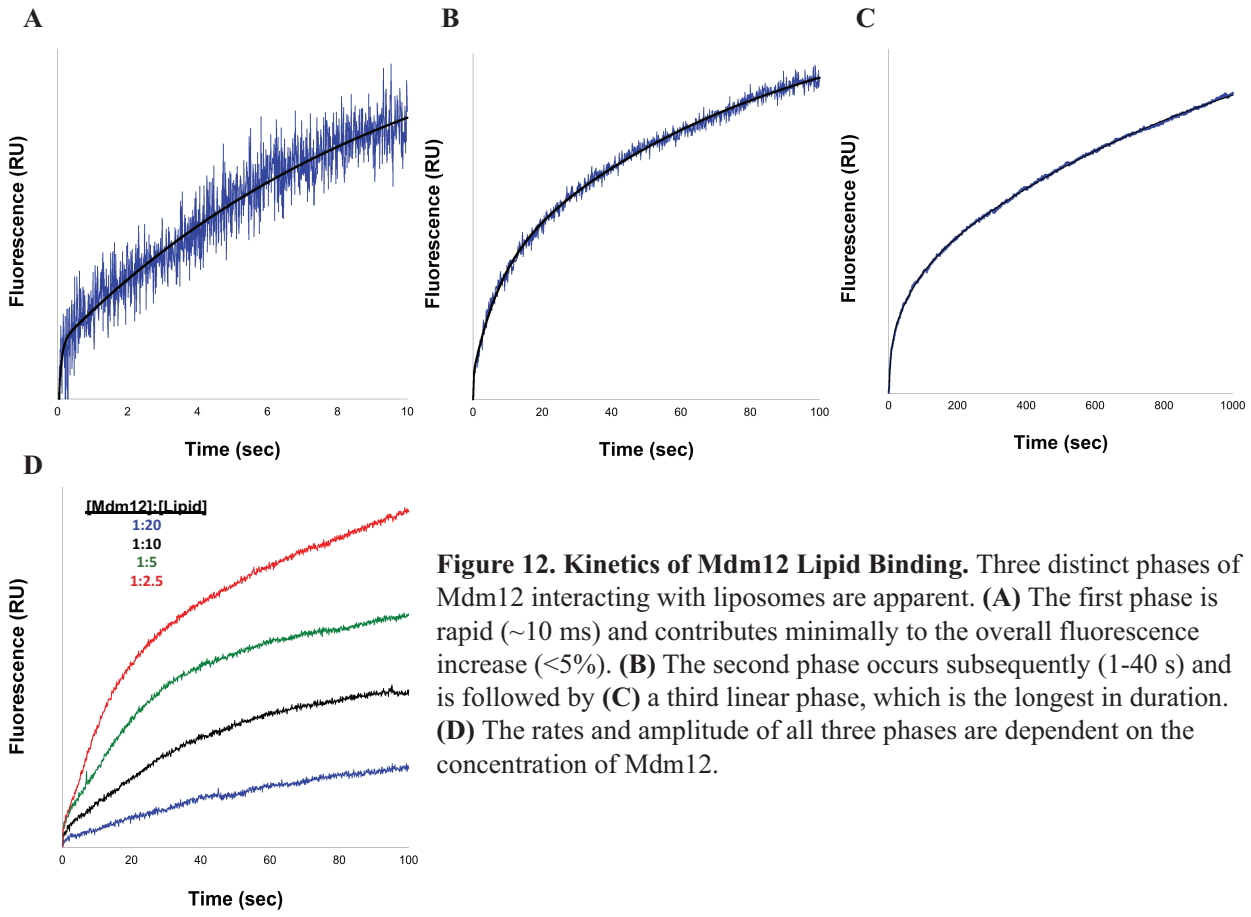

Figure 12. Kinetics of Mdm12 Lipid Binding. Three distinct phases of Mdm12 interacting with liposomes are apparent. **(A)** The first phase is rapid (~10 ms) and contributes minimally to the overall fluorescence increase (<5%). **(B)** The second phase occurs subsequently (1-40 s) and is followed by **(C)** a third linear phase, which is the longest in duration. **(D)** The rates and amplitude of all three phases are dependent on the concentration of Mdm12.

significantly (~50%) to the overall Mdm12-induced fluorescence change (**Fig. 12C**). Importantly, the rate and magnitude of the fluorescence response is dependent on the concentration of Mdm12 added, suggesting that the combined overall reaction is governed by at minimum first order kinetics with respect to the Mdm12 concentration (**Fig. 12D**). However, the fluorescence output from NBD dequenching is a combination of multiple potential reactions (e.g. lipid phase change, Mdm12 lipid-binding). This ambiguity greatly confounds data analysis and makes it difficult to distinguish and characterize each kinetic phase individually.

Stopped-flow measurements also showed that both DTT and calcium affect the kinetics of Mdm12 lipid binding. Pre-incubation of Mdm12 with 1 mM DTT increases the rate and overall magnitude of Mdm12 lipid binding (**Fig. 13A**). Although our finding that Mdm12 dimerization is disulfide-mediated stands in contrast to the β1-strand swap observed in the

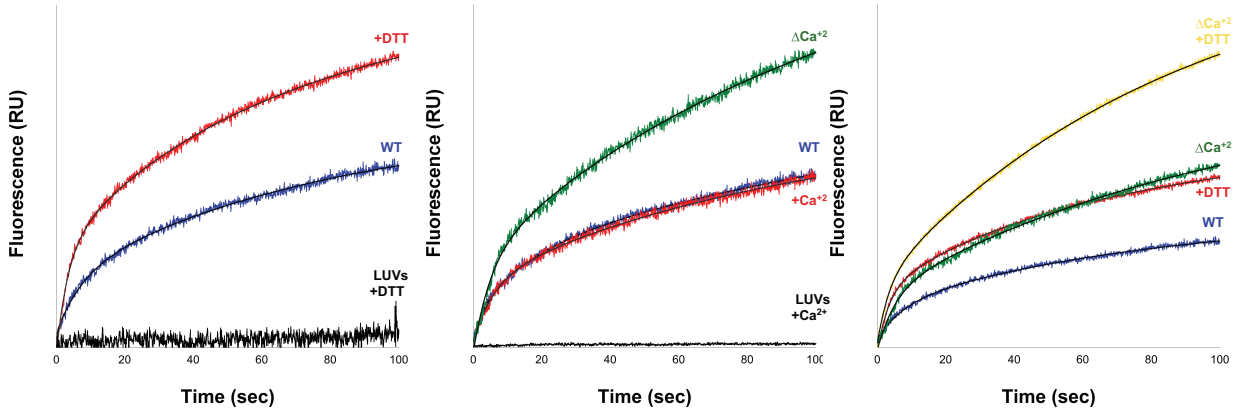

Figure 13. Calcium and DTT affect the kinetics of Mdm12 lipid binding. (A) Mdm12 WT and liposomes of 100% NBD-PE were rapid-mixed at equimolar concentration. In the presence of reductant DTT, the rate of reaction and the amplitude of the overall fluorescence signal was amplified. DTT alone had no effect on the dequenching of NBD fluorescence. **(B)** When calcium is removed by dialysis with EGTA-containing buffer (ΔCa^{+2}), the overall fluorescence signal and the rate of reaction also increase. When calcium is reintroduced the kinetics of interaction are restored to that of Mdm12 WT before dialysis. Calcium alone has no effect on dequenching of NBD fluoresence. **(C)** The absence of calcium and presence of reductant have a combinatorial effect on the kinetics of interaction.

crystal structure, biochemical studies accompanying the structure similarly observed that Mdm12 binds lipids with greater affinity as a monomer rather than a dimer.

Similarly, the removal of calcium (Mdm12 ΔCa^{+2}) also increases the overall reaction rate and fluorescence response (**Fig. 13B**). Upon the reintroduction of calcium (5 μM) to Mdm12 ΔCa^{+2}, the reaction rate and fluorescence signal are restored to wild type levels. Interestingly, Mdm12 ΔCa^{+2} also treated with DTT exhibits a combinatorial effect on reaction kinetics. That is, the presence of reductant in addition to the absence of calcium increases the overall rate and amplitude of the fluorescence response greater than either treatment alone (**Fig. 13C**). Control experiments mixing DTT or calcium with NBD-PE LUVs alone confirm that the fluorescence response is attributable to modulated Mdm12 activity. Calcium is a tightly regulated and potent secondary messenger at MAMs, and this is the first direct biochemical evidence that suggests it may affect MAM function via ERMES.

Because Mdm12 lipid-binding does not reach equilibrium at time intervals accessible by stopped-flow, another NBD dequenching-based method was used to observe the reaction until saturation. A spectrofluorometer was used to collect consecutive wavescans (500-600 nm) of Mdm12 lipid-binding reactions until signal saturation (**Fig. 14**). Binding of Mdm12 WT with NBD-PE LUVs saturated ~60 min (**Fig. 14B**), corresponding to the same time at which the beginning of the second aggregation phase was observed in DLS time course experiments. Time course measurements of Mdm12 treated with 1 mM DTT corroborated stopped-flow results, and relieved NBD self-quenching at a faster rate and induced a larger response than Mdm12 alone (**Fig. 14A/C**). Moreover, DTT-treated Mdm12 lipid-binding reactions took longer to saturate (~120 min vs. ~60 min). Additionally, the emission maximum of NBD in the DTT-treated reaction is further blue-shifted (λ_{em}= 527 nm vs. λ_{em}= 535 nm) (**Fig. 14D**) indicating NBD on average is in a lower dialectric environment. Although not conclusive this could suggest that more total lipid is bound at equilibrium to DTT-treated Mdm12, which would support the previous findings that the Mdm12 monomer binds lipids more readily than the dimer.

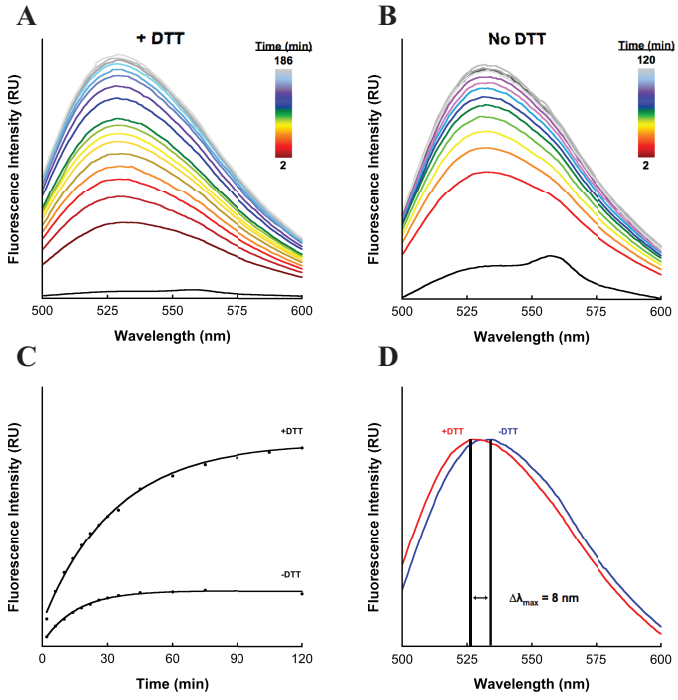

Figure 14. Mdm12 Lipid-Binding Reaction Time Course. Lipid binding reactions were performed (20 nM Mdm12; 0.4 µM NBD-PE) for both Mdm12 WT **(B)** and Mdm12 WT preincubated with DTT before lipid-binding **(A)** and consecutive wavescans were recorded until saturation. Mdm12 preincubated with DTT relieved self-quenching of NBD significantly faster and induced a much larger response (2.4x) than untreated Mdm12 **(C)**. The reaction also proceeded for 186 min until reaching full saturation (*not shown)*, whereas lipid-binding saturated after ~60 min with untreated Mdm12. In both experiments NBD-PE LUVs alone measured a λ_{em}= 557 nm, and a blue shift was observed upon addition of Mdm12. However, the emission maxima differed between DTT (λ_{em}= 527 nm) and untreated Mdm12 (λ_{em}= 535 nm) lipid-binding **(D)**.

Discussion

Because ER-mitochondria contact sites are major conduits of lipid trafficking independent of the endomembrane system, illumination of the molecular basis of ERMES-mediated phospholipid transport is poised to uncover novel concepts in membrane biology. Membrane contact sites are ubiquitous yet also enigmatic. Understanding how the SMP domain-containing subunits of ERMES assemble to recognize, extract, and transport phospholipids could possibly characterize a general mechanism for lipid transport at membrane contact sites in general. To this end, this study sought to investigate the assembly state and lipid binding properties of ERMES subunit Mdm12 in isolation.

Our finding that Mdm12 exists primarily as a dimer in dynamic equilibrium corroborates previous findings[30,31,41]. However, in this study we found Mdm12 oligomerization to be primarily disulfide-mediated and facilitated largely by C92 disulfide bond formation. Of note, our biochemical analyses of Mdm12 association state were performed using a full-length N-terminal His-tagged construct, before structural information was available. Crystal structures show that Mdm12 forms dimers mediated by contacts between conserved β1-strands. Interestingly, a recent structure of Mdm12 demonstrates that β1-mediated dimerization is promiscuous, in that β1-strands can mediate self-association by either strand swapping[30] or asymmetrically with only one strand engaged at the dimer interface (**Fig. 15A/C**)[41]. Additionally, all structures to date show a 'non-crystallographic' dimer mediated by large crystal contact surfaces that exceed the buried surface area of the *bona fide* dimer interface (**Fig. 15B**). The unresolved disordered loop containing C92 is proximal to this interface, and because our construct contains an N-terminal His-tag that likely occludes β1-strand interaction, the dimer observed in this work is likely distinct from that previously investigated.

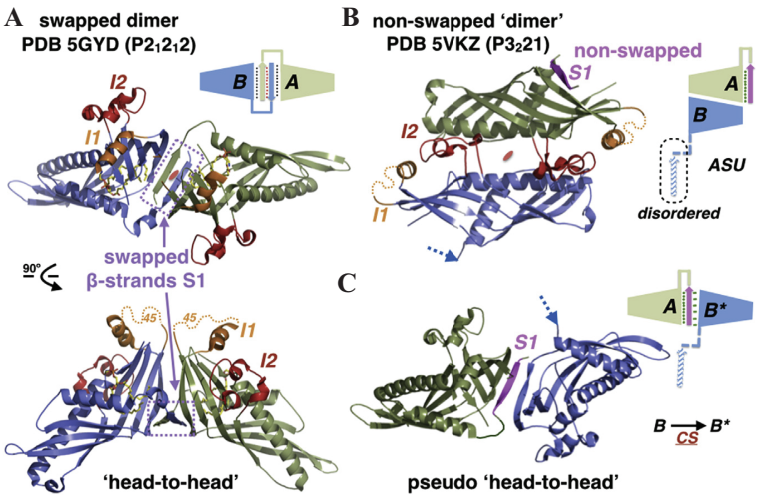

Figure 15. Dimerization interface of Mdm12. (A) β1-strand-swapped dimer previously shown from Jeong et al. (2016). **(B)** Non-swapped/non-crystallographic dimer corresponding to an 'anti-parallel' arrangement along helix H2 proximal to C92. This large contact interface may directly involve C92 and is observed in every Mdm12 structure to date. **(C)** An asymmetric pseudo 'head-to-head' dimer involving only the β1-strand from monomer A.

Figure adapted from AhYoung et al. (2017)

Moreover, all purification and biochemical studies of Mdm12 to date have been performed under highly reducing conditions (2.8 mM[31, 41], and 5 mM[30] BME) and AhYoung et al. (2015) even performed mutagenesis of C92 to improve sample homogeneity for crystallization[41]. Although this disordered region is variable, little is known about the local redox environment at membrane contact sites and it is possible that disulfide-mediated dimerization has physiological function.

Although it is widely assumed that ERMES mediates non-vesicular lipid transport, this study is the first to investigate Mdm12—bilayer interaction and demonstrate the effect of an ERMES subunit on overall bilayer morphology. It is clear from the experimental findings presented above that Mdm12 significantly disrupts the integrity of lipid bilayers composed of NBD-PE. It is important to note that when derivatized with an NBD moiety conjugated to the headgroup PE no longer exhibits polymorphic phase behavior[42-44]. Rather NBD-PE is characterized as a lamellar lipid, hence its ability to form stable bilayers averse to high curvature. Although a molecular interpretation of the mechanism of Mdm12—bilayer interaction is still lacking, the data presented in this study clearly demonstrate the ability of Mdm12 to disrupt lipid

bilayers and induce significant polymorphism. Real-time stopped-flow and DLS measurements also show that reaction progression follows a defined progression of Mdm12-mediated bilayer changes. Taken together we propose a coarse working model for the mechanism of Mdm12 action on lipid bilayers (**Fig. 16**).

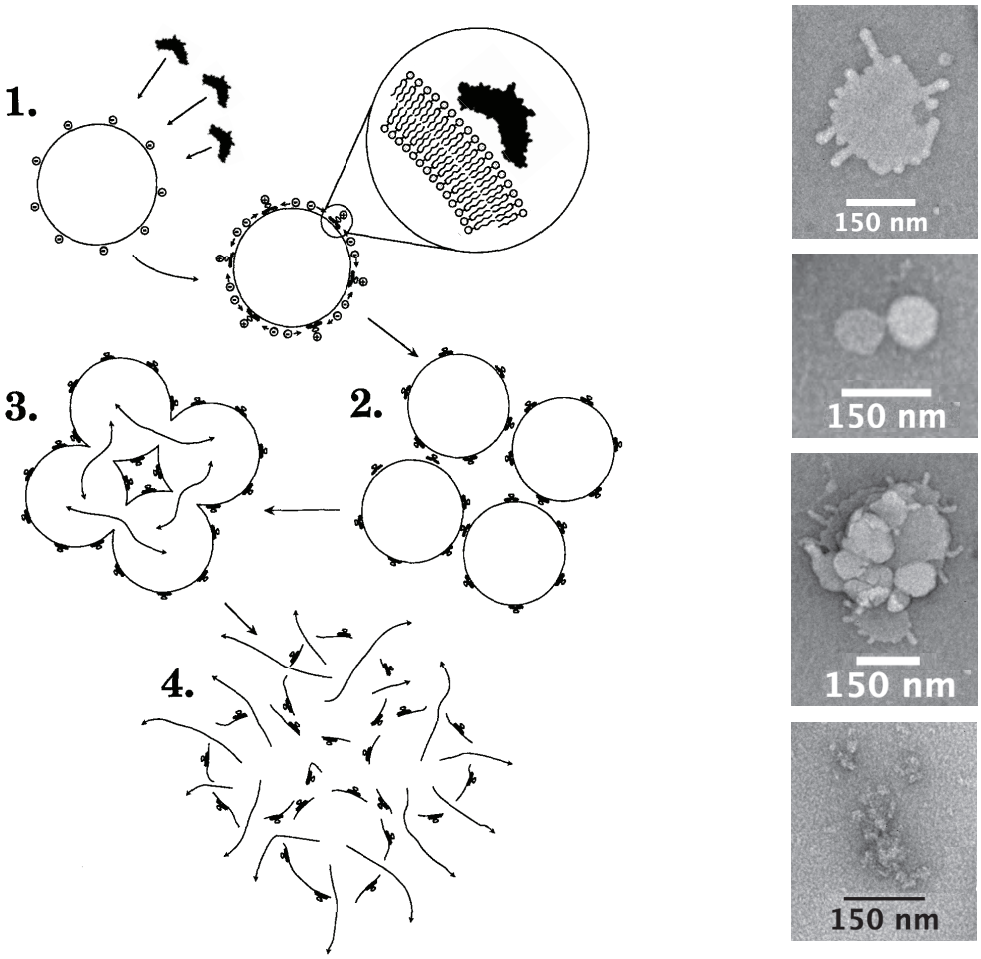

Figure 16. Proposed Model for Mdm12—Bilayer Interaction. In isolation Mdm12 significantly disrupts synthetic bilayers (NBD-PE). These changes occur in distinct phases at different rates. Representative TEM images showing putative Mdm12-induced morphologies corresponding to the propposed model. **(1)** Mdm12 must first interact with the exterior surface of liposomes, however, the specific interactions that mediate association are unknown. **(2)** A small amount of tethering is apparent and aggregation accompanies the destabilization of the bilayer. **(3)** This induces bilayer fusion, and **(4)** subsequent lysis or solubilization. The reaction continues to equilibrium until again aggregate is formed, which may or may not distict from aggregates formed in previous phases.

Schematic adapted from R.I. Abu-Ghazaleh et al. 1992

Mdm12 first binds the exterior leaflet of bilayers likely by a combination of electrostatic and hydrophobic interactions, however the energetic basis of this interaction is unknown. Binding induces liposome clustering and features of membrane tethering, and tubulation is also observed. Bilayer destabilization induces aggregation and fusion of clustered liposomes. As shown using DLS average particle size decreases to the size of Mdm12 alone in solution, possibly indicating membrane solubilization. Although there is no direct evidence of the ability of Mdm12 to breach the lipid bilayer, from TEM images we speculate that the integrity of liposome compartmentalization is compromised. Large granular aggregates are visible in TEM images and could be representative of solubilized lipid—Mdm12 aggregates. Of additional note, stopped-flow measurements showed that calcium modulates the lipid-binding of Mdm12. Because ER-mitochondria contact sites are major conduits for calcium exchange, a deeper understanding of this effect is of particular interest.

These findings stand in apparent contrast to the notion that ERMES facilitates monomeric lipid transport independent of fusion and large-scale membrane morphological changes. Preliminary results have indicated that other SMP domain-containing proteins facilitate lipid transport without concurrent fusion[4]. Mdm12 also bridges the connection between juxtaposed membranes via interaction with Mmm1 and Mdm34. Thus, Mdm12 is assumed to be a transducer of lipid transport and have limited direct contact with the bilayer. It is very likely that Mdm12 interacts differently in physiological context. Regardless, these results provide a starting point to address the major question of how SMP domain-containing proteins are able to extract and deposit lipids into adjacent bilayers at membrane contact sites.

Appendix A

Analysis of SS-31 Lipid Binding Kinetics

I. Abstract

The SS-31 peptide is a synthetic tetrapeptide containing an alternating cationic-aromatic motif that represents a first-in-class therapeutic which restores compromised mitochondrial bioenergetics (**Fig. A1A)**. By modulating the ultrastructure of the mitochondrial inner membrane (IMM) SS-31 is thought to restore oxidative phosphorylation, leading to clinical improvements in a diverse set of complex diseases. However, the biophysical mode of SS-31 action remains uncharacterized. Despite bearing a +3 net charge at physiological pH, SS-31 is readily taken up by all tested cell types to date and targeted specifically to the IMM[46]. Intriguingly, there is no apparent receptor or transporter-mediated requirement for uptake or localization, and the distribution of SS-31 within mitochondria was found to be membrane potential independent[47].

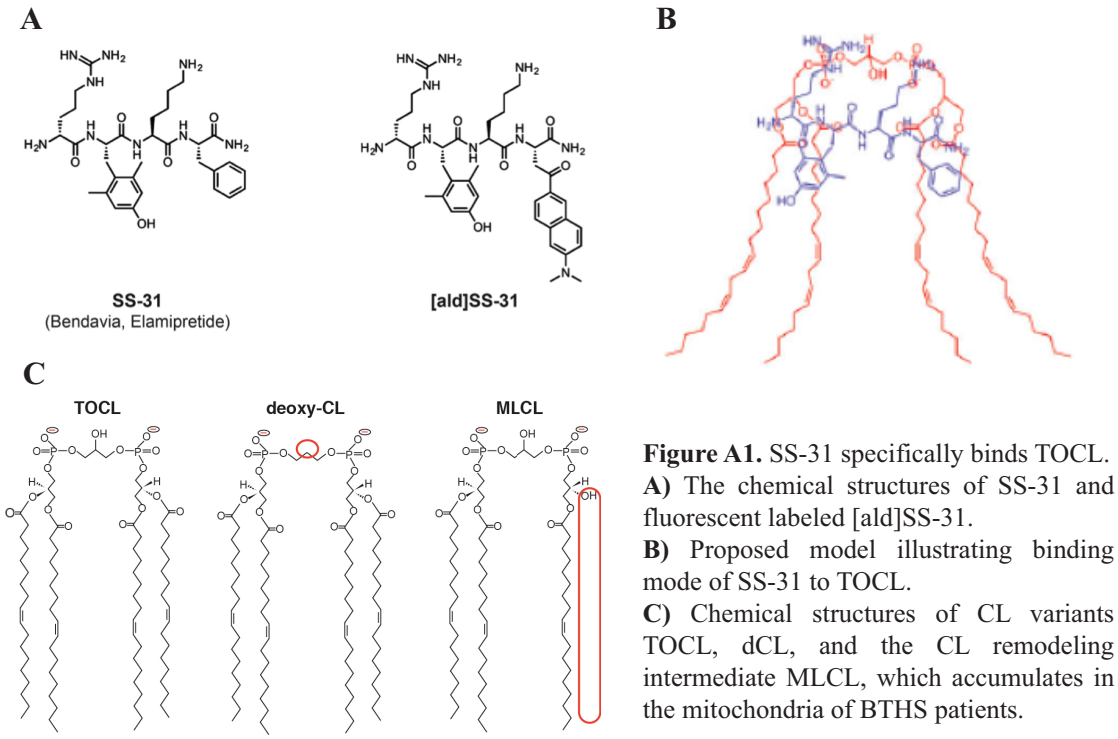

Figure A1. SS-31 specifically binds TOCL. **A)** The chemical structures of SS-31 and fluorescent labeled [ald]SS-31. **B)** Proposed model illustrating binding mode of SS-31 to TOCL. **C)** Chemical structures of CL variants TOCL, dCL, and the CL remodeling intermediate MLCL, which accumulates in the mitochondria of BTHS patients.

Using a combination of nuclear magnetic resonance (NMR), Rayleigh scattering, and fluorescence-based approaches, it was later revealed that SS-31 selectively binds to cardiolipin (CL), a unique phospholipid which has two phosphate headgroups connected by a single glycerol moiety, and is found principally in the IMM[48]. From these data it was proposed that SS-31 and tetraoleoyl cardiolipin (TOCL) interact at a 1:1 molar ratio, in which electrostatic interactions between the two cationic residues of one SS-31 molecule and the two phosphate head-groups of TOCL align the aromatic residues for hydrophobic interaction with the acyl chain region (**Fig. A1B**). This study explores the potential use of SS-31 as a therapeutic for Barth Syndrome (BTHS), a multisystemic disorder caused by mutation of the gene encoding tafazzin, the transacylase responsible for the remodeling of acyl chains during TOCL biosynthesis. BTHS patients show decreased levels of CL and an accumulation of the biosynthetic intermediate monolysocardiolipin (MLCL) (**Fig. A1C**). The following kinetic analysis of the interactions between SS-31 and CL variant-containing bilayers points to the potential use of SS-31 to treat BTHS, and gives key mechanistic insights into the mode of SS-31 binding.

II. Materials and Methods

Steady-state fluorescence. Stock solution of [ald]SS-31 (250 μM) was prepared by re-suspension of lyophilized peptide in reaction buffer (20 mM HEPES [pH 7.5], 100 mM NaCl). CL-containing LUV stock solutions (250 μM) were prepared as described above. Samples were mixed at each respective concentration LUVs and incubated for 20 min then transferred to 250 μL quartz sample cuvettes (4x4-mm). Measurements were made using a Spex Fluorolog 3-22 spectrofluorometer (HORIBA Jobin-Yvon) with double-grating excitation/emission monochrometers (Ex: λ = 360 nm, Em: λ = 400-600 nm, 2-nm bandpass). ΔEmission at 461 nm

was used to define specific binding, and the data were fit to the Hill-equation (**Eqn. 1**) to extrapolate binding parameters.

$$\theta = \frac{[\mathrm{L}]^n}{K_d + [\mathrm{L}]^n} \quad \text{(Equation 1)}$$

Stopped-flow fluorescence. Pre-steady-state kinetics experiments were performed with an SX-20 instrument (Applied Photophysics, UK). Samples were excited at 360 nm and emission was detected using a 400 nm long-pass cutoff filter. Peptide and LUVs were loaded into a 1.0 mL syringes at double the final reaction concentration, respectively, and equal volumetric mixing ratio of [ald]SS-31: LUVs was used. The final concentration of [ald]SS-31 was constant in all experiments (1 μM) and the concentration of CL-variant LUVs was titrated. All experiments were performed in reaction buffer (20 mM HEPES [pH 7.5], 100 mM NaCl). Data were analyzed using SX Pro-Data Viewer (Applied Photophysics, UK). Triplicate fluorescent transients from a single experiment were averaged and fit to multiexponential curves, in which an additional exponential term was added to account for photobleaching. The rate of this fixed additional term was determined by peptide : reaction buffer equal-mixing control experiments.

III. Results

Biphasic membrane binding by [ald]SS-31

The association between [ald]SS-31 and CL-containing bilayers was found to be a biphasic process characterized by two distinct kinetic phases, an initial rapid phase followed by a subsequent slow phase (**Fig. A2**). The rate of the fast phase (k_1) linearly increased with accessible lipid concentration upon titration with liposomes containing TOCL, dCL, or MLCL.

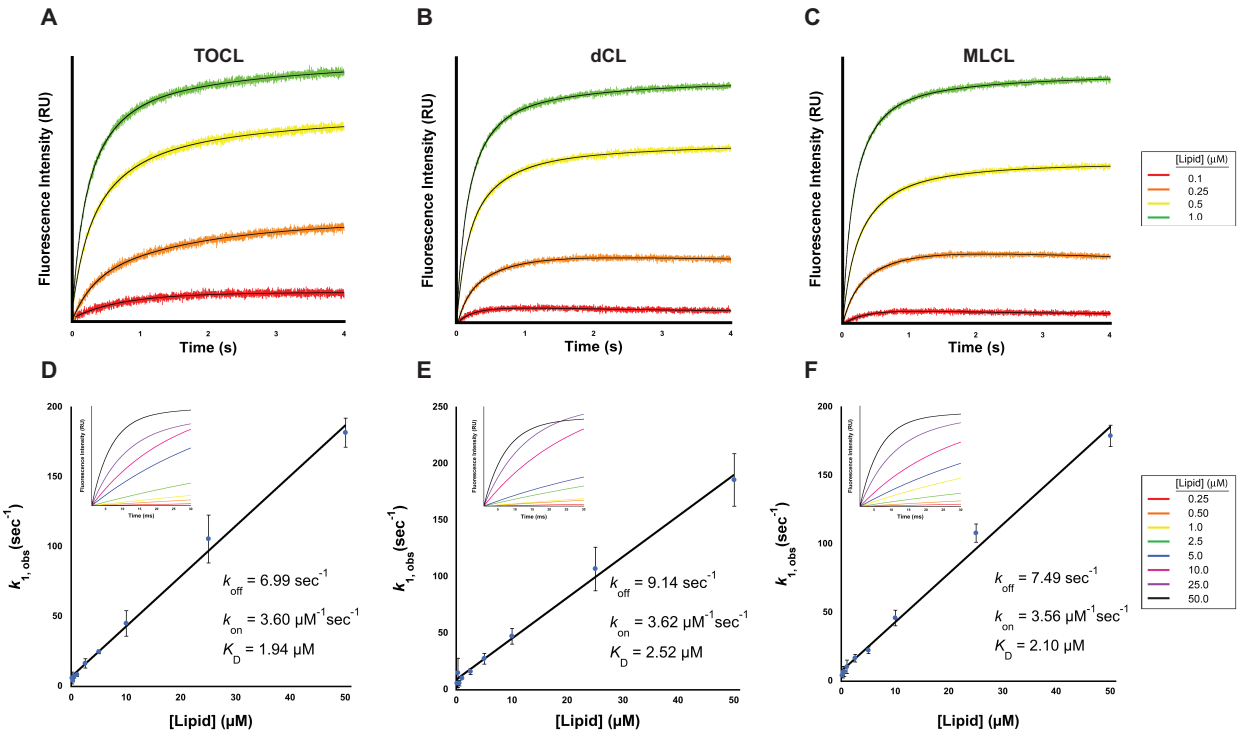

Figure A2. Kinetics of SS-31 binding to CL-containing bilayers. (A-C) Representative stopped-flow fluorescence transients of [ald]SS-31 (1 μM) added to liposomes containing 50 mol% of CL variants at the indicated lipid concentration. Binding of [ald]SS-31 to liposomes is biphasic. **(D-F)** Association (k_{on}) and dissociation (k_{off}) rate constants determined by pseudo first-order approximation for the first phase of [ald]SS-31 binding to CL variants. Insets show the first 30 ms binding transients identifying the first phase.

Moreover, the rate of the fast phase contributed significantly more to the overal fluorescence increase (~60-95%). The forward rate of the rapid association phase (k_{+1}) was approximately 3.60 $\mu M^{-1} sec^{-1}$ for each CL-variant, whereas the reverse rate of the phase (k_{-1}) differed between species. The differences in the affinity constants (K_D) that were extrapolated from pre steady-state kinetic measurements are hence, most largely attributable to variations in the reverse rate constant k_{-1}. The slow rate, however, was not dependent on the lipid concentration and remained approximately constant at ~0.4 s^{-1} (not shown) for all CL species, indicating this is either a zero-order process or a first-order process subsequent to the first concentration-dependent reaction. Steady-state measurements also showed close agreement with pre-steady state results, and indicate that [ald]SS-31 binds with low micro-molar affinity to bilayers containing TOCL, dCL, and MLCL (**Fig. A3).**

IV. Discussion

Taken together, these results can be represented by a minimal model for the kinetic mechanism of [ald]SS-31 bilayer association:

$$P + L \underset{k_{-1} = 3.60\ \mu M^{-1}sec^{-1}}{\overset{k_{+1} = 0.052\ \mu M^{-1}sec^{-1}}{\rightleftharpoons}} P{:}L \rightarrow P{:}L^{*}$$

where the kinetic parameters shown are those measured for TOCL-containing bilayers, and the peptide and liposomes are represented by P and L, respectively. P:L represents the product of the initial rapid reaction, and P:L* represents the product of the subsequent slow reaction phase. The fast phase likely correspond to an initial phase bilayer interaction mediated by electrostatic and hydrophobic interactions between the basic and aromatic residues of SS-31. In contrast the slower phase may correspond to the alignment of peptides within the bilayer *via* peptide—peptide interactions, or represent alterations in bilayer properties such as interfacial packing.

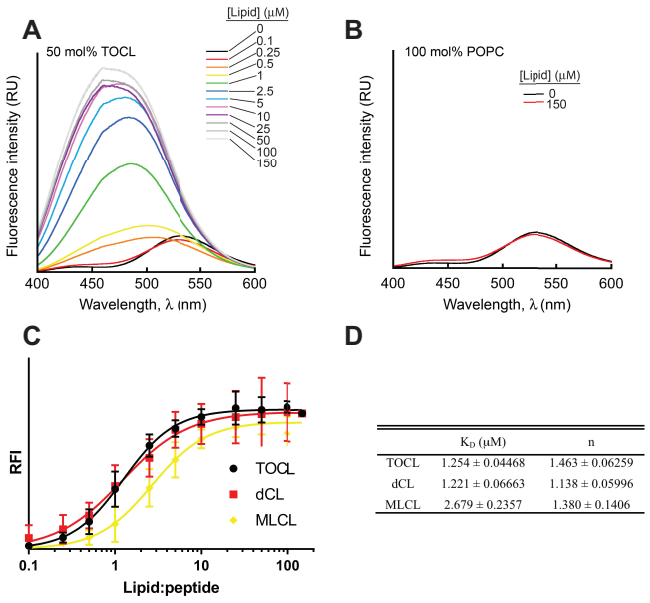

	K_D (μM)	n
TOCL	1.254 ± 0.04468	1.463 ± 0.06259
dCL	1.221 ± 0.06663	1.138 ± 0.05996
MLCL	2.679 ± 0.2357	1.380 ± 0.1406

Figure A3. Equilibrium binding of SS-31 to CL-containing bilayers. **(A)** Emission spectra of [ald]SS-31 (1 μM) incubated to equilibrium (20 min) with liposomes containing 50 mol% TOCL of 100 mol% POPC **(B)**. **(C)** Saturation binding curves of [ald]SS-31 with increasing concentrations of liposomes containing 50 mol% of the respective CL variants shown. Curves were fit to Hill expansions of Langmuir binding isotherms, and fitted parameters were reported with the standard deviation and as the mean of triplicate experiments **(D)**.

Of particular note SS-31 binds MLCL-containing bilayers with similar affinity to TOCL-containing bilayers, supporting the notion that SS-31 may well be effective in targeting the IMM of mitochondria in Barth Syndrome patients, and possibly in ameliorating the characteristic bioenergetics deficiencies. Moreover, the kinetics of [ald]SS-31 binding to CL-containing bilayers are generally the same for TOCL, dCL, and MLCL, in which there is rapid phase dependent on lipid concentration followed by a subsequent slow phase that does not depend on

lipid concentration. Although k_{-1} differed between CL-variants, the other measured parameters k_{-1} and k_2 were consistently similar. Interestingly the Hill coefficients for TOCL and MLCL binding were greater than that measured for dCL, and this may represent subtle differences in head-group dependent SS-31—CL interactions. Changes in head-group geometry and chemistry may also affect interfacial packing and the alignment of peptides already bound to the bilayers.

References

1. Robertson, J.D. (1960). The molecular structure and contact relationships of cell membranes. *Prog Biophys Mol Biol* 10: 289-297.

2. Friedman, J.R., Lackner, L.L., West, M., DiBenedetto, J.R., Nunnari, J., Voeltz, G.K. (2011). ER tubules mark sites of mitochondrial division. *Science* 334: 358-362.

3. Alder, N.N. (2011). Biogenesis of Lipids and Proteins within Biological Membranes. *The structure of Biological Membranes* (ed. Yeagle, P.L.) 315-317 (CRC, 2011).

4. Helle, S. C. J., Kanfer, G., Kolar, K., Lang, A., Michel, A. H., & Kornmann, B. (2013). Organization and function of membrane contact sites. *BBA - Molecular Cell Research*, *1833*(11), 2526–2541

5. Giacomello, M., & Pellegrini, L. (2016). The coming of age of the mitochondria—ER contact: a matter of thickness. *Cell Death Differ 23*(9), 1417–1427.

6. Horvath , S.E., Daum, G. (2013). Lipids of mitochondria. *Prog Lipid Res* 52 , 590-614.

7. Trotter , P.J., Pedretti , J., Voelker , D.R. (1993). Phosphatidylserine decarboxylase from Saccharomyces cerevisae. Isolation of mutants, cloning of the gene, and creation of a null allele. *J Biol Chem* 286 , 21416-24.

8. Lev, S. (2012). Nonvesicular Lipid Transfer from the Endoplasmic Reticulum. *Cold Spring Harbor Perspectives in Biology*, *4*(10).

9. Denton, R.M. (2009). Regulation of mitochondrial dehydrogenases by calcium ions. *Biochim Biophys Acta* 1787, 1309-16.

10. Hajnoczky, G., Hager, R. & Thomas, A.P. (1999). Mitochondria suppress local feedback activation of inositol 1, 4, 5-triphosphate receptors by Ca^{2+}. *J Biol Chem* 274, 14157-62.

11. Bernardi, P. & Rasola, A. (2007). Calcium and cell death: the mitochondrial connection. *Subcell Biochem* 45, 481-506.

12. Area-Gomez, E., Del Carmen Lara Castillo, M,. Tambini, M.D., Guardia-Laguarta, C., de Groof, A.J., Madra, M., et al. (2012). Upregulated function of mitochondria-associated ER membranes in Alzheimer disease. *EMBO* 31: 4106–4123.

13. Ottolini, D., Cali, T., Negro, A., Brini, M. (2013). The Parkinson disease-related protein DJ-1 counteracts mitochondrial impairment induced by the tumour suppressor protein p53 by enhancing endoplasmic reticulum-mitochondria tethering. *Hum Mol Genet* 22: 2152–2168.

14. Giorgi, C., Bonora, M., Sorrentino, G., Missiroli, S., Poletti, F., Suski, J.M., et al. (2015). p53 at the endoplasmic reticulum regulates apoptosis in a Ca2+-dependent manner. *PNAS* 112: 1779–1784.

15. Csordas, G., Renken, C., Varnai, P., Walter, L., Weaver, D., Buttle, K.F., et al. (2006). Structural and functional features and significance of the physical linkage between ER and mitochondria. *J Cell Biol* 174: 915–921.

16. Csordas, G., Varnai, P., Golenar, T., Roy, S., Purkins, G., Schneider, T.G., et al. (2010). Imaging interorganelle contacts and local calcium dynamics at the ER-mitochondrial interface. *Mol Cell* 39: 121–132.

17. Giacomello, M., Drago, I., Bortolozzi, M., Scorzeto, M., Gianelle, A., Pizzo, P., et al. (2010). Ca^{2+} hot spots on the mitochondrial surface are generated by Ca2+ mobilization from stores, but not by activation of store-operated Ca^{2+} channels. *Mol Cell* 38: 280–290.

18. Clapham, D.E. Calcium signaling. (2007). *Cell* 131, 1047-1058.

19. Baughman, J.M. et al. (2011). Integrative genomics identifies MCU as an essential component of the mitochondrial calcium uniporter. *Nature* 476, 341-345.

20. De Stefani, D., Raffaeollo, A., Teardo, E., Szabo, I. & Rizzuto, R. (2011). A forty-kilodalton protein of the inner membrane is the mitochondrial calcium uniporter. *Nature* 476, 336-340.

21. Kornmann, B. et al. (2009). An ER-mitochondria tethering complex revealed by a synthetic biology screen. *Science* 325, 477-81.

22. Kornmann, B., Osman, C., and Walter, P. (2011). The conserved GTPase Gem1 regulates endoplasmic reticulum-mitochondria connections. *PNAS* 108, 14151-56.

23. Kojima, R., Endo, T., & Tamura, Y. (2016). A phospholipid transfer function of ER-mitochondria encounter structure revealed in vitro. *Scientific Reports 6*(1), 1-9.

24. Ellenrieder, L., ski, L. U. O. N., Becker, L., ger, V. K. U., Mirus, O., Straub, S. P., et al. (2016). Separating mitochondrial protein assembly and endoplasmic reticulum tethering by selective coupling of Mdm10. *Nature Communications*, *7*, 1–14.

25. Voss, C., Lahiri, S., Young, B. P., Loewen, C. J., & Prinz, W. A. (2012). ER-shaping proteins facilitate lipid exchange between the ER and mitochondria in S. cerevisiae. *Journal of Cell Science*, *125*(20), 4791–4799.

26. Lang, A., Peter, A. T. J., & Kornmann, B. (2015). ER–mitochondria contact sites in yeast: beyond the myths of ERMES. *Current Opinion in Cell Biology*, *35*, 7–12.

27. Herrera-Cruz, M. S., & Simmen, T. (2017). Of yeast, mice and men: MAMs come in two flavors. *Biology Direct*, 1–21.

28. Kopec, K.O., Alva, V. & Lupas, A.N. (2010). Homology of SMP domains to the TULIP superfamily of lipid-binding proteins provides a structural basis for lipid exchange between ER and mitochondria. *Bioinformatics* 26, 1927-1931.

29. Kopec, K.O., Alva, V. & Lupas, A.N. (2011). Bioinformatics of the TULIP domain superfamily. *Biochem Soc Trans* 39, 1033-8.

30. Jeong, H., Park, J., & Lee, C. (2016). Crystal structure of Mdm12 reveals the architecture and dynamic organization of the ERMES complex. *EMBO Reports*, *17*(12), 1857–1871.

31. AhYoung, A. P., Jiang, J., Zhang, J., Khoi Dang, X., Loo, J. A., Zhou, Z. H., & Egea, P. F. (2015). Conserved SMP domains of the ERMES complex bind phospholipids and mediate tether assembly. *PNAS*, *112*(25), E3179–E3188.

32. Nguyen, T. T., Lewandowska, A., Choi, J.-Y., Markgraf, D. F., Junker, M., Bilgin, M., et al. (2012). Gem1 and ERMES Do Not Directly Affect Phosphatidylserine Transport from ER to Mitochondria or Mitochondrial Inheritance. *Traffic*, *13*(6), 880–890.

33. Schauder, C.M., Wu, X., Saheki, Y., Narayanaswamy, P., Torta, F., Wenk, M.R., De Camilli, P., Reinisch, K.M. (2014). Structure of a lipid-bound Extended-Synaptotagmin indicates a role in lipid transfer. *Nature*, 510: 552-

34. Qiu, X., Mistry, A., Ammirati, M.J., Chrunyk, B.A., Clark, R.W., Cong, Y., Culp, J.S., Danley, D.E., Freeman, T.B., Geoghegan, K.F. (2007). Crystal structure of cholesteryl ester transfer proteins reveals a long tunnel and four bound lipid molecules. *Nat Struct Mol Biol* 14:106-113.

35. Beamer, L.J., Carrol S.F., Eisenberg, D. (1997). Crystal structure of human BPI and two bound phospholipids at 2.4 angstrom resolution. *Science* 276:1861-1864.

36. Zinser, E., Sperka-Gottlieb, C.D., Fasch, E.V., Kohlwein, S.D., Paltauf, F., & Daum, G. (1991). Phospholipid synthesis and lipid composition of subcellular membranes in the unicellular eukaryote Saccharomyces cerevisiae. *Journal of Bacteriology,173*(6), 2026-2034.

37. Stewart, J. (1980). Colorimetric determination of phospholipids with ammonium ferrothiocyanate. *Analytical Biochemistry 104*(1): 10-14.

38. Friesner, R.A., et al. (2004) Glide: A New Approach for Rapid, Accurate Docking and Scoring. *J. Med. Chem.* 47, 1739-1749.

39. Norris, A.W.,Cheng, L., Giguère, V., Rosenberger, M., Li, E. (1994). Measurement of subnanomolar retinoic acid binding affinities for cellular retinoic acid binding proteins by fluorometric titration, *BBA—Prot. Struct. & Mol. Enzymology 1209*(1): 10-18.

40. Abu-Ghazaleh, R.I., Gleich, G.J., Prendergast, F.G. (1992). Interaction of Eosinophil Granule Major Basic Protein with Synthetic Lipid Bilayers: A Mechanism for Toxicity. *J. Membrane Biol.* 128, 153-164

41. AhYoung, A.P., Lu, B., Cascio, D., Egea, P.F. (2017) Crystal structure of Mdm12 and combinatorial reconstitution of Mdm12/Mmm1 ERMES complexes for structural studies. *Biochem and Biophys Res Comm*, 488: 129-135.

42. Maier, O., Oberle, V., Hoekstra, D. (2002). Fluorescent lipid probes: some properties and applications (a review). *Chemistry and Physics of Lipids*. 116: 3-18.

43. Chernomordik, L.V., Zimmerberg, J., (1995). Bending membranesto the task: structural intermediates in bilayer fusion. *Curr. Opin. Struct. Biol.* 5: 541–547.

44. Pecheur, E.I., Sainte-Marie, J., Bienvenue, A., Hoekstra, D. (1999). Peptides and membrane fusion: towards an understanding of the molecular mechanism of protein-induced fusion. *J. Membrane Biol.* 167: 1–17.

45. Reinisch K.M., De Camilli, P. (2015). SMP-domain proteins at membrane contact sites: Structure and function. *BBA - Molecular and Cell Biology of Lipids 1861*(8): 924-927.

46. Szeto, H., Birk, A. (2014). Serendipity and the Discovery of Novel Compounds That Restore Mitochondrial Plasticity. *Clinical pharmacology and therapeutics 96*(6): 672-683.

47. Zhao, K., Zhao, G., Wu, D., Soong, Y., Birk, A.V., Schiller, P.W., Szeto, H.H. (2004). Cell-permeable Peptide Antioxidants Targeted to Inner Mitochondrial Membrane inhibit Mitochondrial Swelling, Oxidative Cell Death, and Reperfusion Injury. *Journal of Biological Chemistry. 279*(33): 34682-90.

48. Birk, A.V., Liu, S., Soong, Y., Mills, W., Singh, P., Warren, J.D., Szeto, H.H. (2013). The Mitochondrial-Targeted Compound SS-31 Re-Energizes Ischemic Mitochondria by Interacting with Cardiolipin. *Journal of the American Society of Nephrology*, 24(8), 1250-126.